

Microstructure and mechanical properties of in-situ TiB₂/TiC/(Ti, Nb)C reinforced Inconel 718 coating by laser direct energy deposition

Chuang Guan^a, Ying Chen^a, Fanwei Meng^a, Liaoyuan Chen^b, Zhelun Ma^a, Tianbiao Yu^{a,*}

^a School of Mechanical Engineering and Automation, Northeastern University, Shenyang 110819, China

^b School of Mechatronics Engineering, Henan University of Science and Technology, Luoyang, China

ARTICLE INFO

Keywords:

Inconel 718 coating
Laser DED
In-situ synthesis
Loop (Ti, Nb)C phase
Microstructure
Mechanical properties

ABSTRACT

Inconel 718 coating has been applied in various applications such as aviation impellers and gas turbines due to its excellent tensile properties, high impact toughness, corrosion resistance, and creep resistance. However, its low hardness and poor wear resistance restrict its broader applications. In this study, laser directed energy deposition (DED) is utilized to in-situ synthesize TiB₂, TiC, and (Ti, Nb)C ceramic phases, which improves the mechanical properties of the Inconel 718 coating. The effect of five coatings with different Ti and B₄C contents on phase, microstructure, microhardness, scratch, and wear resistance was studied. Gibbs free energy (*G*), SEM, EDS, and EBSD were used to analyze experimental phenomena. The results showed that TiB₂, TiC, and (Ti, Nb)C ceramic phases were in-situ synthesized. The (Ti, Nb)C phase with a loop shape was around TiC phase and TiB₂ phase, which were found on the Laves phase and at grain boundaries. The formation and positional relationship of the Nb atom and Ti atom in MC (refer to TiC and (Ti, Nb)C) crystal structure have been investigated. The distribution of Ti atom and Nb atom within the MC crystal structure, as well as their effect on *G*, have also been analyzed. The mechanical properties of Inconel 718 coating have been significantly improved as a result of fine-grain strengthening, solid solution strengthening, and second-phase strengthening. The addition of B₄C + Ti content can considerably enhance the microhardness of Inconel 718 coatings by 62.96 %, and the fitting function of powder content and microhardness has been obtained. The deformation resistance is increased, and the toughness is reduced. The deformation of the scratch has been translated from plastic deformation to shear deformation. In addition, the wear mechanism of the coating changed from adhesive wear to abrasive wear, and the minimum wear rate is $1.70 \times 10^{-4} \text{ mm}^3/\text{Nm}$. This study

proposes a novel approach for improving the mechanical properties of Inconel 718 coating, as well as provides guidelines for coating preparation.

1. Introduction

Inconel 718 stands out from Ni-based superalloys for its outstanding properties, making it highly desirable across numerous industries [1]. In addition to its primary strengths (high-temperature resilience, creep resistance, and superior corrosion/oxidation protection), it offers weldability, ease of fabrication, and remarkable versatility. Inconel 718 has become an ideal choice for manufacturing complex components, customized products, and demanding applications where reliability and performance are crucial [2]. The laser directed energy deposition (DED) is an efficient method for preparing Inconel 718 coatings. However, the Inconel 718 coating has several disadvantages, including poor wear resistance and low hardness. Therefore, it is necessary to improve the

performance of Inconel 718 coating so that it can be used in a wider range of applications and working environments. The traditional methods to reinforce the Inconel 718 coating include heat treatment [2] and ultrasonic treatment [3]. However, these methods have some drawbacks that cannot be ignored, such as being environmentally unfriendly, inefficient, and so on [4,5].

In the past decade, many scholars focused on the study of reinforced coatings with additional new phases by laser DED. Among the many reinforced phases, SiO₂, WC, TiC, and other ceramic phases with high hardness and excellent chemical stability have become research hotspots. For instance, Gao et al. [6] conducted real-time Operando X-ray diffraction to capture and monitor the solidification process. The results indicated that the ceramic phase MC hinders grain coarsening during

* Corresponding author.

E-mail address: tianbiaoyudyx@gmail.com (T. Yu).

<https://doi.org/10.1016/j.matchar.2024.114709>

Received 17 October 2024; Received in revised form 20 December 2024; Accepted 30 December 2024

Available online 31 December 2024

1044-5803/© 2025 Elsevier Inc. All rights are reserved, including those for text and data mining, AI training, and similar technologies.

solidification, which highlights its crucial role in enhancing material hardness. Zheng et al. [7] explored how the TiB_2 ceramic phase refines grains and increases the hardness of Inconel 718 coating. The study also reported that heat treatment has negligible effects on the hardness of Inconel 718 coatings. Based on the above, the ceramic phase positively affects the reinforced coatings. However, the ceramic phases with large sizes can increase the porosity and reduce bonding ability and so on. For instance, Ning et al. [8] illustrated that the addition of SiC ceramic particles improves the microstructure and hardness, while reducing the bonding ability between Inconel 718 metal matrix composite and substrates. Bhatnagar et al. [9] reported that TiC ceramic phase size affects laser beam absorption and dilution rate. Thermodynamic analysis indicates that most ceramic phases have positive G , making them unable to decompose during laser direct energy deposition (DED) [10,11]. This property implies physical contact between the ceramic phases and the matrix powder. The differing thermal expansion coefficients of different powders result in unstable wettability and poor bonding performance [12]. The bonding performance is crucial for the mechanical properties of composite coatings [13,14]. These issues can lead to coating failure and performance degradation, and the ceramic particle separation from

the matrix is a serious consequence during mechanical loading [15,16].

In order to address these issues, several studies have been conducted to investigate the advantages of using in-situ ceramic phases by laser DED. This approach enhances thermal stability and interfacial compatibility, improving stress transfer [17,18]. Recently, hot ceramic phases like TiC, TiB_2 , and their corresponding binary phases have been studied extensively. Chen et al. [19] used Ni45, Ti, and graphite to in-situ synthesize TiC ceramic phases in a gradient coating on ductile cast iron using laser DED. The gradual increase in microhardness is due to improved solid solution, grain refinement, and dispersion strengthening facilitated by the larger in-situ synthesized TiC phase. Gao et al. [20] found that in-situ synthesized ceramic phases have better physical and mechanical properties compared to the individual ceramic phases. Zhao et al. [21] confirmed that composite carbides offer distinct advantages over single carbides, with (Nb, Ti)C carbide showing significantly enhanced hardness, brittleness, and interface binding energy, as well as reduced lattice mismatch with Fe. Increasing the Ti content shifts carbides from eutectic to primary. Although the in-situ synthesis of TiC- TiB_2 has been studied in Fe-based and Ni-based alloys, little research has been conducted on superalloy powder Inconel 718, which has a complex

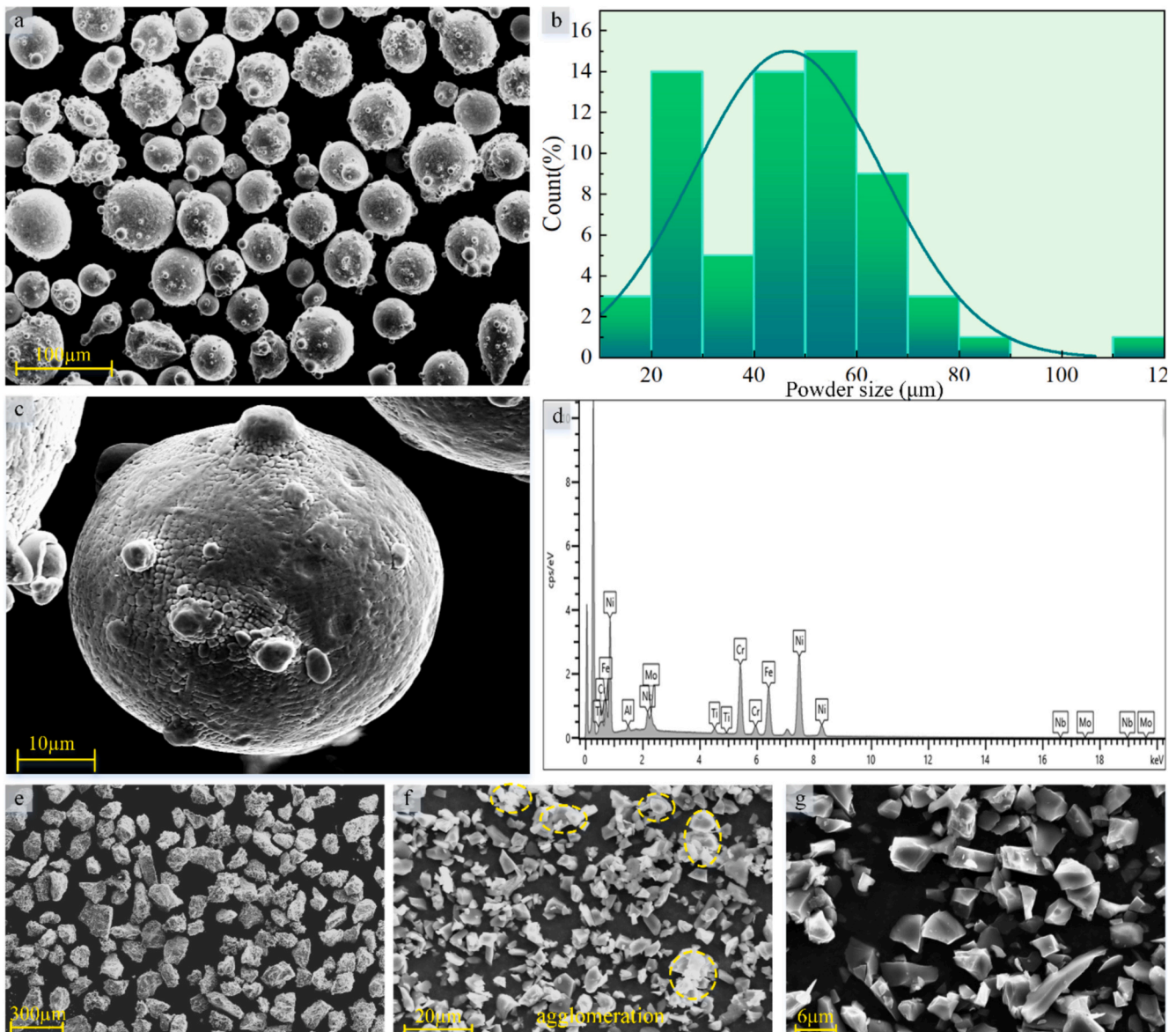


Fig. 1. (a) SEM mapping of Inconel 718; (b) Size distribution of Inconel 718; (c) Magnified view of Inconel 718 particle; (d) Chemical composition of Inconel 718; (e) SEM mapping of pure Ti powder; (f) SEM mapping of pure B_4C powder; and (g) Magnified view of B_4C particles.

element composition and high-temperature resistance. Research on the in-situ synthesis of loop (Ti, Nb)C phase is also little.

In this paper, the porosity, crack, phase, microstructure, microhardness, scratch, and wear resistance were analyzed for five coatings with different Ti and B₄C contents. The porosity and crack were analyzed via the optical microscopic. The reaction order of in-situ synthesized was revealed by thermodynamic analysis. Additionally, SEM, EDS, and EBSD were used to investigate the microstructure and distribution of in-situ synthesized ceramic phases. The microhardness, scratch performance, and wear resistance of the Inconel 718 coatings containing different Ti and B₄C contents had been thoroughly investigated. This study offers valuable insights for improving coating quality and repairing techniques to achieve superior mechanical properties.

2. Materials and methods

2.1. Materials

Inconel 718 (made in Chengdu Koton Alloy Co. Ltd., China, GH4169) was utilized in this paper. The SEM mappings and magnified view of Inconel 718 are shown in Fig. 1. The powder size can be found in Fig. 1(b), with an average particle size of 46.66 μm. The main chemical composition is shown in Fig. 1(d). The particles are uniform, elliptical, and well-defined without agglomeration. Pure B₄C and Ti powders were added to strengthen Inconel 718 coatings. The geometric morphology of pure Ti powder (99.5 % purity) is visible in Fig. 1(e). The geometry of pure B₄C (98 % purity) powder with a diameter of ≤73 μm (see Fig. 1f), while the magnified view of the powder is given in Fig. 1(g), exhibiting its small size in diameter.

The material of the substrate for this experiment is 40Cr, with the dimension of 100 mm × 100 mm × 10 mm. Table 1 lists the detailed chemical components of Inconel 718 powder and 40Cr substrate. The molar ratio of in-situ TiC and TiB₂ was 1:1, so the mass ratio of pure B₄C to pure Ti powder was 1:3. Table 2 shows the powder proportions used in the coating preparation.

2.2. Laser DED process

The laser DED system consists of a 6-axis KUKA robot (R16–2), a coaxial powder feeding nozzle (RC5) attached to the robot's end effector, a powder feeder that pushes powder into the system via a rotating powder disc, a water cooler, a laser generator, and a robot control system. The IPG YLR-500 fiber laser generates the laser beam, which acts on the workpiece surface through the coaxial powder feeding nozzle. The defocus distance between the nozzle and the workpiece is 15.0 mm. Ar gas serves as both shielding gas (15 L min⁻¹) and powder delivery gas (8 L min⁻¹).

Fig. 2 illustrates the experimental and detection processes for the ceramic reinforcement coatings. The experimental steps are shown in Fig. 2(a–g). Firstly, the additional powder and Inconel 718 were proportionally weighed. Subsequently, the Al₂O₃ balls were added to the mixing powder, and the ball mill was set to 30 rpm for 2 h. The mixed powder was dried at 100 °C for 4 h. Finally, the designed scanning strategy was used to control the KUKA robot precisely during the coating preparation process. The experimental procedure and principle are detailed in Fig. 2(f) and (g), while Fig. 2(h) shows the final coating. The process parameters for the coatings are the powder feed rate of 0.8 r/min, the scanning speed of 8 mm/s, and the laser powder of 400 W.

These samples were wire-cut to obtain cross-sections and end faces.

Table 1

Chemical composition of the substrate and Inconel 718 powder (wt%).

	Ni	Cr	Si	C	Mn	Co	Cu	Nb	Mo	Al	Ti	P	S	Fe
Inconel 718	52.6	19.6	0.07	0.03	–	0.14	0.09	5.06	3.02	0.4	0.94	0.01	–	Bal
40Cr	0.25	0.95	0.28	0.4	0.65	–	–	–	0.08	–	–	0.03	0.03	Bal

Table 2

The powder proportions for the coating preparation.

Ingredient (wt%)	Inconel 718	Ti	B ₄ C
Sample S0	100.00	0.00	0.00
Sample S1	95.00	3.75	1.25
Sample S2	90.00	7.50	2.50
Sample S3	85.00	11.25	3.75
Sample S4	80.00	15.00	5.00

The surfaces of these samples were polished using SiC sandpapers (240 to 3000 grit) and diamond paste (2.5 μm grain diameter) for 30 min. Subsequently, these samples were etched with aqua regia for 20–60 s. Finally, the processed samples underwent various tests, such as SEM, EDS, EBSD, and microscopy (OLS4100). SEM and EBSD were employed to analyze the microstructure and grain orientations. The Vickers indentation tester (300 g loading force, 10-s dwell time) was used to measure the microhardness. The tribological tests were performed on a multifunctional material surface performance tester to evaluate wear properties. The grinding ball was made of 99.5 % pure Al₂O₃ with a diameter of 5 mm and a microhardness of 1650 HV. The cone angle of the diamond indenter for the scratch test was 120°. The indenter was pressed into the composite coating at a speed of 50 N·min⁻¹ with a slip distance of 2 mm.

3. Results and discussion

3.1. Porosity and crack

The pores and cracks of the coatings can be effectively inspected through the dye penetration inspection. Fig. 3 shows the original and penetration morphologies. The results indicate that there are no pores on the surface of the sample S0. However, the number and size of pores gradually increase as the B₄C + Ti content increases (Fig. 3g, h, i, and j).

For further research, the optical microscopic images of pores and cracks in S0, S1, S2, S3, and S4 are depicted in Fig. 4. One reason for pore generation can be attributed that the shielding gas and delivery gas do not escape during the experimental process [22]. Another reason is that the pores are generated by the chemical reactions between the composite powder and air. The pores are small and regular in sample S0. However, the pores become bigger as the B₄C + Ti content increases. The relationship between the porosity and powder content was fitted, which can be expressed as follows:

$$P = 1.218 + 2.578X - 0.224X^2 + 0.007X^3 \quad (1)$$

Where P is the porosity and $X\%$ is the Ti + B₄C powder content in mass percentage. The coefficient of determination (R-squared) is 0.9914 (see Fig. 5a). The shape of pores in sample S2 became increasingly irregular as the Ti + B₄C content increased. Magnified views of I and II in Fig. 4(f) demonstrate differences in pore sizes. The average values of the pore width and length follow the equations:

$$W = 21.33 + 12.63X \quad (2)$$

$$K = 19.77 + 12.44X \quad (3)$$

Where K and W are the length (R-squared 0.9711) and width (R-squared 0.9523) of pores, respectively. Length and width have similar variation trends, indicating that the size of pores becomes uneven and large. It can be found in Fig. 5(d) that the data of width/length ratio

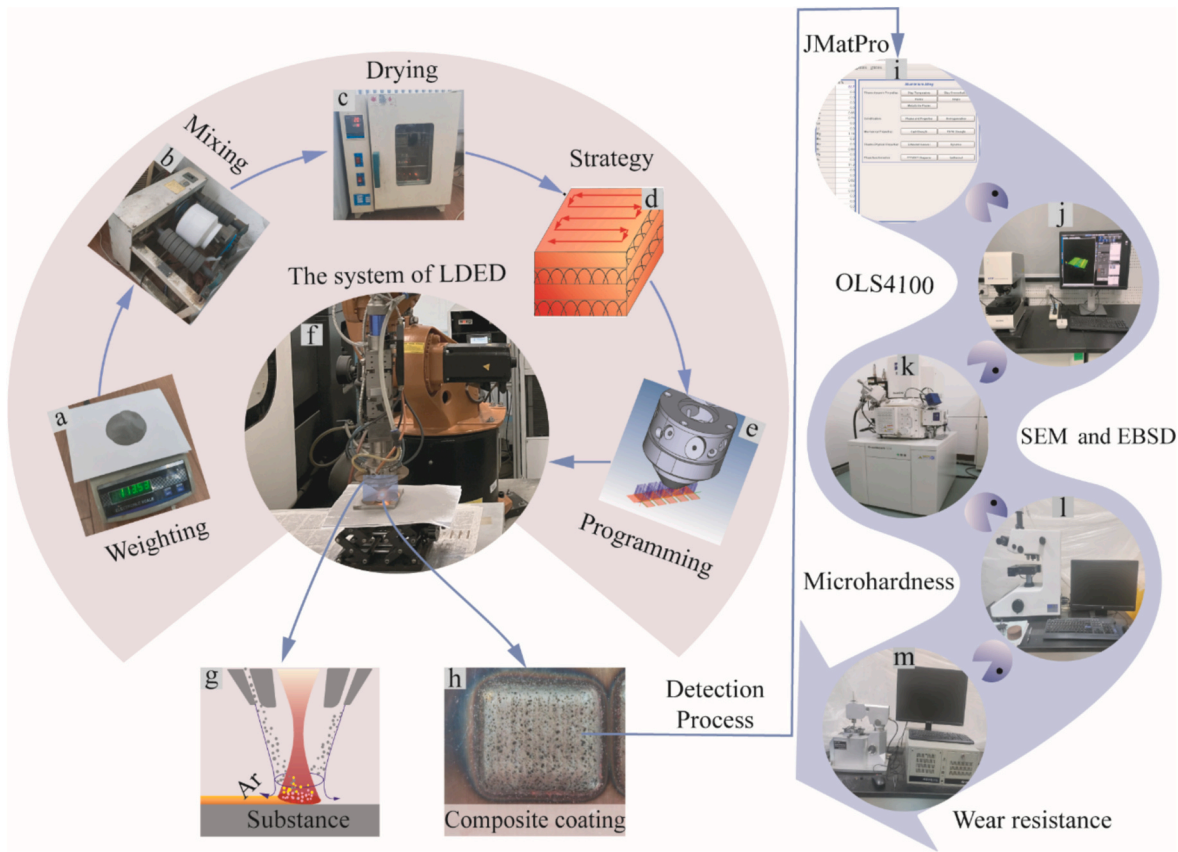


Fig. 2. The experimental process and testing process of ceramic reinforcement coatings.

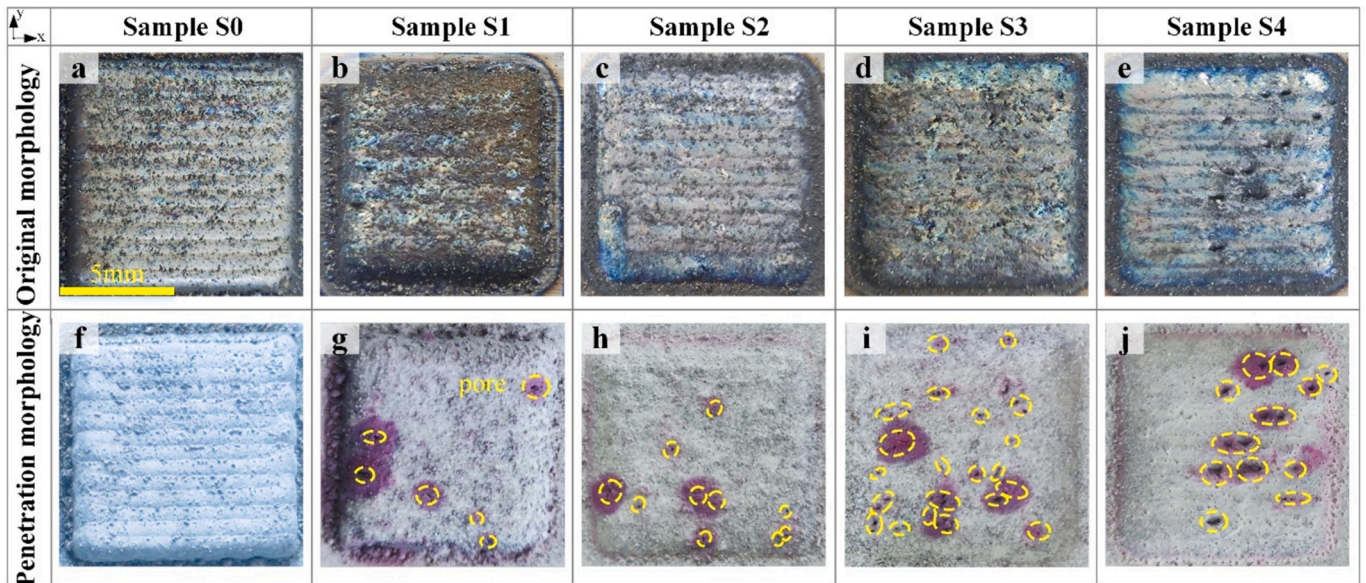


Fig. 3. The original and penetration morphologies of S0, S1, S2, S3, and S4.

becomes more dispersed. This indicates that the pores have become irregular. These irregular-shaped pores are derived from the unmelted powder during the laser DED [23,24]. When the laser energy density is constant, the number of unmelted ceramic particles increases with the addition of powder increases. Due to their melting point is high. Therefore, the size and number of irregular pores increased.

Generally, residual stress is caused by rapid cooling rate during the laser DED, which induces cracks in the coating [25]. Pores, unmelted

powders, coarse grains, impurities, element segregation, and ceramic powder all may become the crack initiation point [26,27]. During the solidification of coating, the bigger residual tensile stress is generated at the crack initiation site than at other sites. The schematic diagram of crack initiation by pores is given in Fig. 6. The generated pores often have a stress concentration, allowing crack initiation and propagation during the solidification of laser DED [28]. As the size of the pores increases, the stress concentration also increases. Defects such as irregular

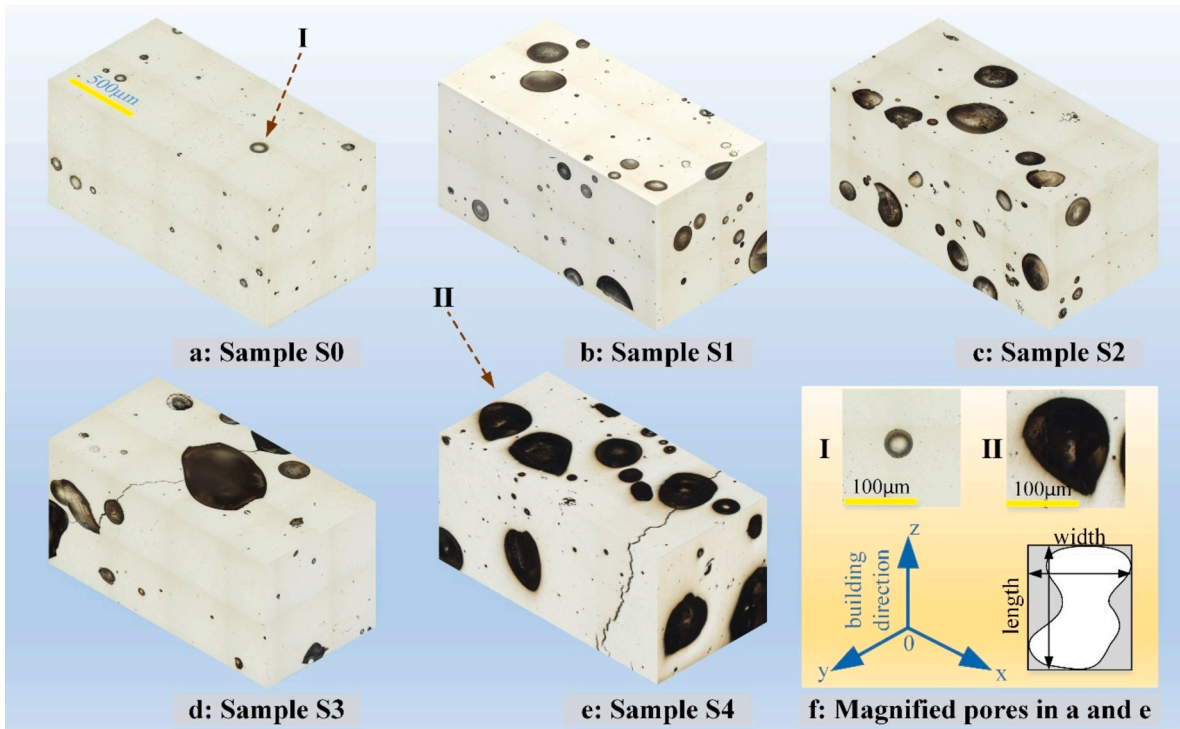


Fig. 4. The distribution of pores and cracks inside samples.

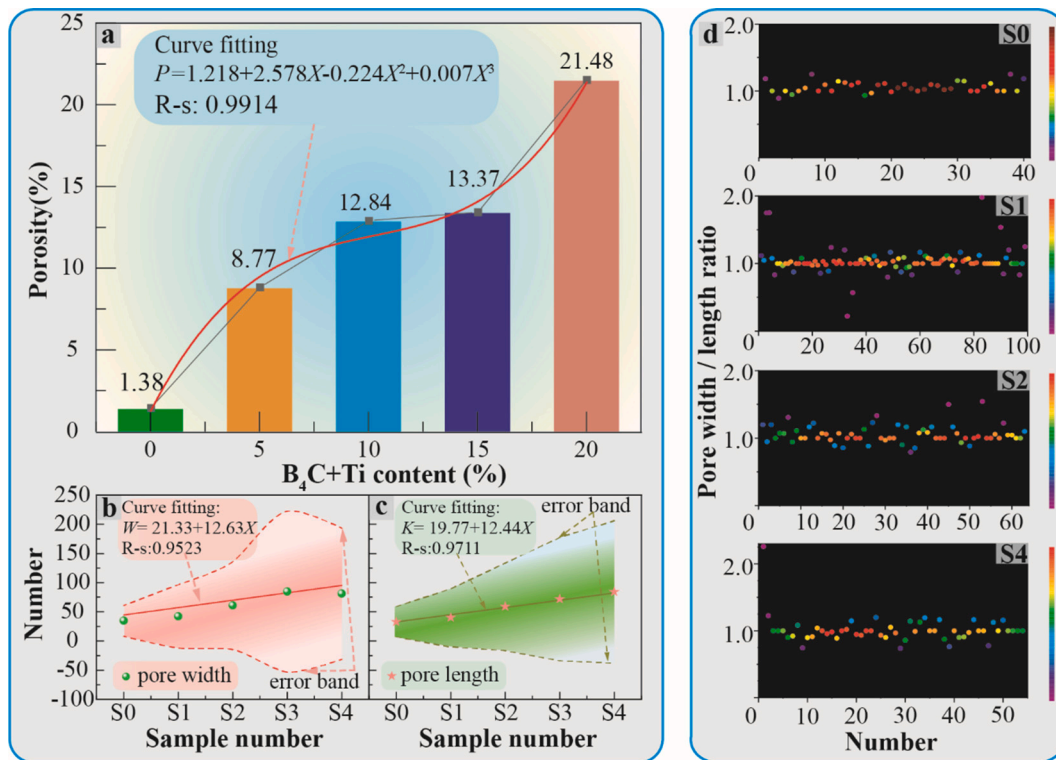


Fig. 5. (a) The porosity of the samples; (b) The average values of pore width; (c) The average values of pore length; and (d) The point density map of pore width/length ratio.

pore morphology, unmelted powder, ceramic powder, coarse grain, and impurity can form crack initiation. Then, the cracks propagate through grain boundaries, especially the loosely packed grain boundaries, until the residual stresses are released. Because the grain boundaries have insufficient strength, the propagation of the crack is promoted. The B_4C

powder can lead to the agglomeration of composite powder, preventing the powder flowability. So, the unmelted powder is generated during the solidification. Meanwhile, it becomes stress concentration points. The ceramic powder, whose physical parameter is significantly different from the Inconel 718 coating, becomes the crack initiation. Therefore, as

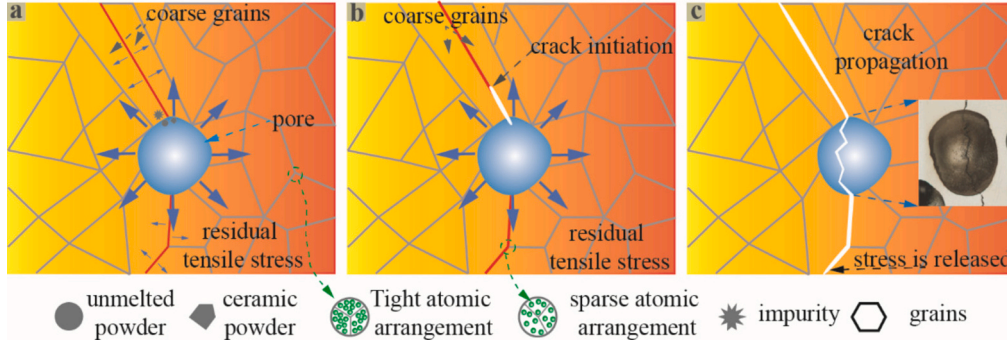


Fig. 6. Schematic diagram of crack initiation by pores: (a) the pore in the coating; (b) the crack initiation; and (c) the crack propagation.

the $B_4C + Ti$ content reaches 15 wt%, the crack is formed (see Fig. 4 d and e).

3.2. Thermodynamic analysis

This paper analyzes the chemical reactions and reaction order during the solidification based on the thermal property module of the “NiFe Based Superalloy” in JMatPro. The thermodynamic calculations in JMatPro are based on CALPHAD technology, with the judgment criterion being the minimization of G . Two principles of CALPHAD technology for a system to reach equilibrium under constant temperature and pressure are: (1) the total G reaches a minimum value of G_{min} , and (2) the chemical potential of each component is equal in all phases.

$$\begin{cases} \frac{\partial G_m(\alpha)}{\partial X_i} = \frac{\partial G_m(\beta)}{\partial X_i} \\ \mu_i(\alpha) = \mu_i(\beta) \end{cases} \quad (4)$$

$$G_m = \sum_i X_i G_i^0 + RT \sum_i X_i \ln X_i + \sum_i \sum_j X_i X_j \sum_v \Omega_v (X_i - X_j)^v \quad (5)$$



Where, Eq. (4) assumes the presence of component i in both the α phase and β phase. Here, G_m represents the molar Gibbs free energy of each phase, μ denotes the chemical potential, X_i stands for the molar fraction of component i , X_j represents the molar fraction of component j , Ω_v signifies the interaction coefficient, R denotes the gas constant, T represents the temperature, and v represents volume. The first term in Eq. (5) represents the sum of molar Gibbs free energies of pure components, the second term signifies the increase in free energy due to ideal mixing entropy, and the third term indicates the excess free energy caused by deviation from a perfect solution. The chemical reactions are inferred as follows:

In reaction 2, M represents Ti and Nb. The G of these phases is shown in Fig. 7. When G is negative, the reaction occurs as the system tends towards the lower energy states. Fig. 7(a) shows that several phases are synthesized spontaneously due to the negative value of G . TiB_2 phase would be synthesized priorly due to the lowest G value. According to this rule, The reaction order is reaction 1–2–4–3, successively. The G values of TiB_2 (S1-S4) are consistent (Fig. 7b), indicating the rise of $B_4C + Ti$ content doesn't affect the G of TiB_2 phase. At the same temperature, as $B_4C + Ti$ content changes, the G value of the TiC phase changes significantly (Fig. 7c). When the temperature exceeds 500 °C, the G value slightly fluctuates with the increase of $B_4C + Ti$ content. During the laser

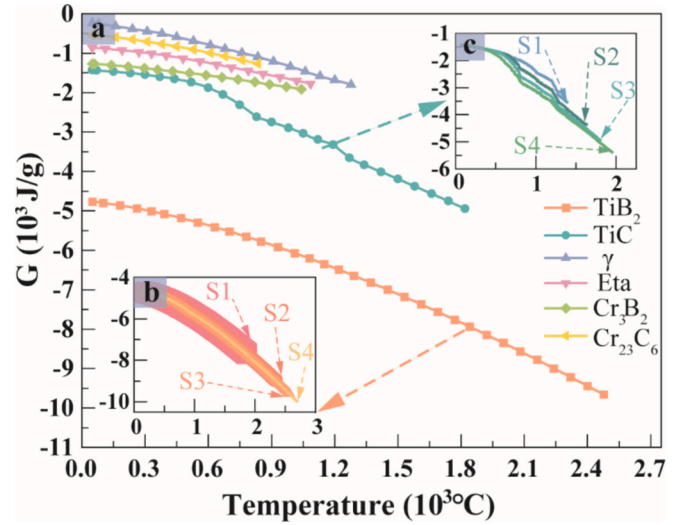


Fig. 7. (a) The G value of possible reactions in the sample S3, (b) The G value of MC in the different samples; and (c) The G value of TiB_2 in the different samples.

DED process, the Ti element priorly combines with the B element to synthesize TiB_2 and then reacts with C to synthesize TiC . Moreover, the C element also reacts with the Nb element of the Inconel 718 to synthesize NbC or (Ti, Nb)C. Ti and Nb, both Group 4B elements, have good solubility due to their similar crystal structures and atomic sizes [29]. Therefore, the TiC , NbC, and (Ti, Nb)C can be synthesized. The different distribution and ratio of Ti atom and Nb atom in the MC Crystal structure affect the G value (see Fig. 7c). There is a noticeable change among samples S1, S2, and S3. However, samples S3 and S4 are similar. Because the Nb content in Inconel 718 is constant and low, when the additional $B_4C + Ti$ content reaches 15 wt% (Sample S3), the Nb elements are reacted sufficiently. So, the G of MC in samples S3 and S4 are similar. Therefore, the influence of Nb content on G value would be diminished. TiC and NbC carbides have the same structure in the Fm-3 m space group, with eight atoms per unit cell, comprising four metal atoms and four C atoms [30]. Ti atoms can be substituted with Nb atoms based on their number, which can be represented as NbC, $(Ti_{0.25}Nb_{0.75})C$, $(Ti_{0.5}Nb_{0.5})C$, $(Ti_{0.75}Nb_{0.25})C$, and TiC . Their crystal structures can be found in Fig. 8.

3.3. Microstructure characterization

The BSE and EDS mappings of C, B, Fe, Mo, Ti, Ni, and Nb in sample S4 are shown in Fig. 9. Ti-Nb-C-B aggregates to form reinforced spots, indicating that the reinforcement phases are synthesized. To further analyze the elemental distribution, Fig. 9 shows the microstructure and

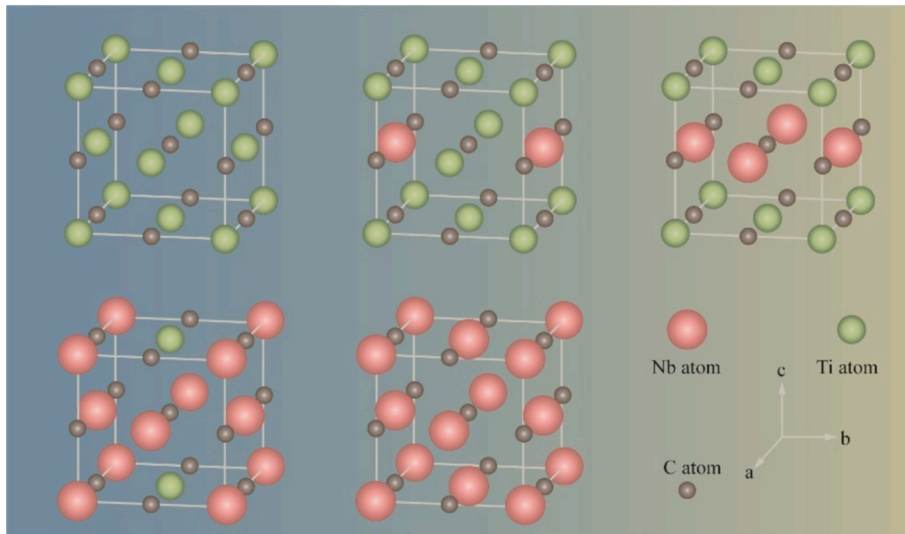


Fig. 8. The crystal structure of the MC phase.

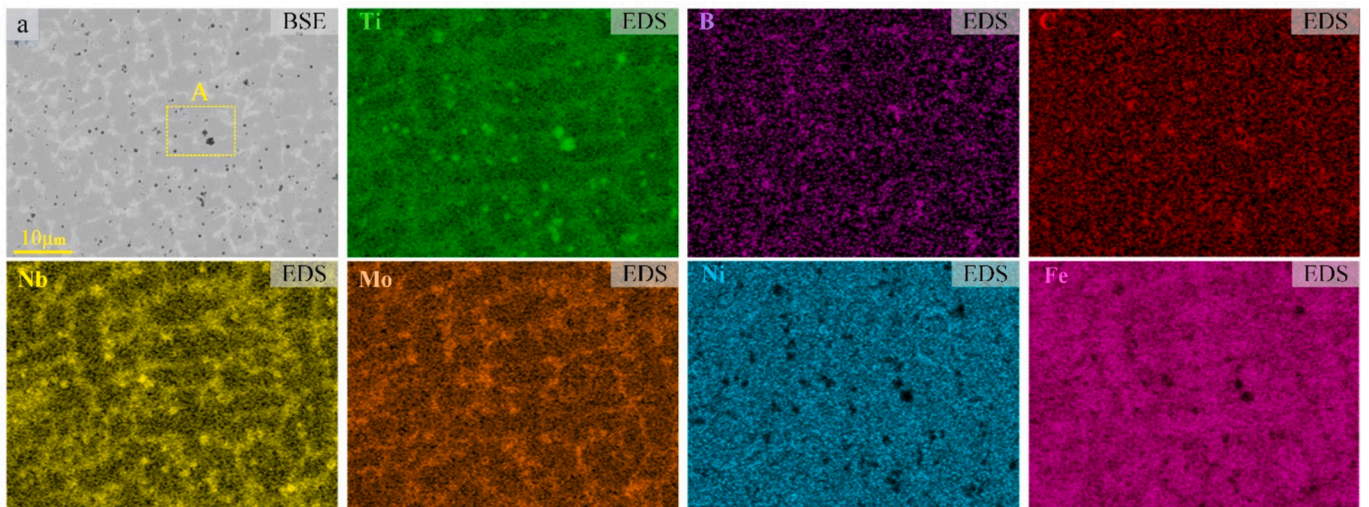


Fig. 9. The main elements distribution of Ti, C, B, Ni, Fe, Mo, and Nb in S4 coating.

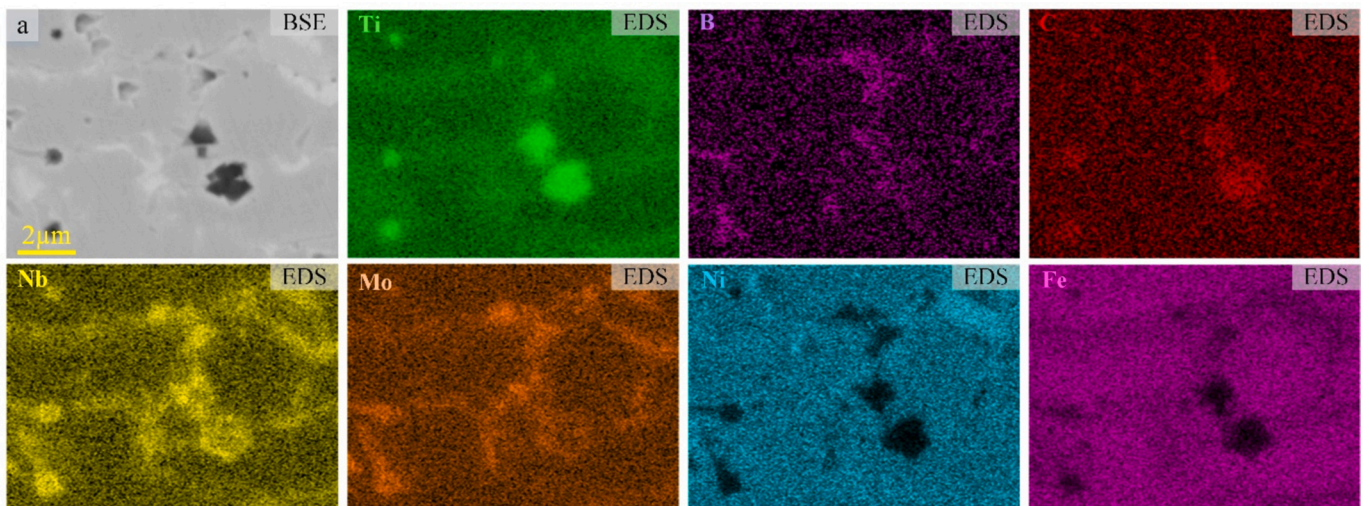


Fig. 10. BSE and EDS mappings of the magnified region A in Fig. 9(a).

corresponding mappings of magnified region A in Fig. 8 (a). The black and gray of irregularly shaped phases were observed in Fig. 10(a). Ti and C were distributed in the central region of the reinforcement phases, while Nb, B, and Mo were distributed on the periphery of the reinforcement phases.

Fig. 11 shows the SEM micrographs of samples and the corresponding points distribution of EDS. The coating consists of a gray matrix phase, black ceramic phases, and white ceramic phases. A bright continuous bonding line at the bond region between the substrate and the coating was observed, which indicates good metallurgical bonding [31]. The addition of B_4C and Ti powder does not affect the bonding performance. The columnar dendrites which are predominantly perpendicular to the bond region are observed. The growth direction of columnar crystals was along the temperature gradient [32,33]. The $B_4C + Ti$ increase results in a higher quantity and larger size of black ceramic phases in the coating (Fig. 11b, e, h).

The EDS analysis and details of these ceramic phases can be found in Table 3. Fig. 11(a) shows that sample S2 is mainly composed of a [Fe—Ni] solid solution, a small white-gray block, a long white-gray rod-shaped block, and a small gray circular block. The [Fe—Ni] solid solution is the γ phase [34]. In the small gray circular block (point 1), there is a significant increase in B, C, Ti, and Nb content, indicating the synthesis of ceramic phases TiB_2 and (Ti, Nb)C. TiC and NbC are similar specifically in lattice constants, atomic radii, and electronegativities [35,36]. Therefore, Ti and Nb atoms are allowed to be substituted in the carbide crystal structure, leading to the synthesis of the dual-phase ceramic of

(Ti, Nb)C, rather than that of the simple-phase ceramic of TiC and NbC [21]. The Fe + Ni content at point 1 is 23.06 %. Therefore, point 1 consists of the γ , TiB_2 , and (Ti, Nb)C. The long white-gray rod-shaped block (point 2) also shows an increase in B, C, Ti, and Nb content, though it is less pronounced than at point 1. Therefore, the region of Point 2 is most likely composed of γ , TiB_2 , and (Ti, Nb)C. The [Fe—Ni] solid solution content at point 2 is 39.66 %, which is higher than that at point 1, resulting in fewer ceramic phases. In addition, the Mo content at points 1 and 2 is significantly higher than that in the original powder, indicating that Mo promotes ceramic phase synthesis [37]. The region of point 3 is composed of the small white-gray phases. Due to the increase in C and B contents and the slight change in Ti and Nb contents, the small white-gray phases could be inferred to be a Cr_3B_2 and γ [38].

As can be seen from Fig. 11(d, g), with the variation of $B_4C + Ti$ content, the phase morphology and element distribution were also changed. The ceramic phases gradually reinforced. Sample S4 mainly consists of γ phase, white-gray long strips, irregular white-gray small rhombic blocks, gray blocks, and black circular blocks. The atomic percentage of C in the black circular block (point 4) is 29.40 % C and 34.13 % Ti, indicating a nearly 1:1 ratio. The EDS and SEM results suggest that the region of point 4 is an in-situ synthesized coarse TiC ceramic phase. The high Nb content indicates the synthesis of TiC and (Ti, Nb)C ceramic phases. The TiC block was encircled by a gray block (point 5). The EDS analysis shows that the atomic percentages of Ti and B are 17.45 % and 32.29 %, respectively, which is close to 1:2. It indicates that TiB_2 phase has been synthesized. The previous study [39]

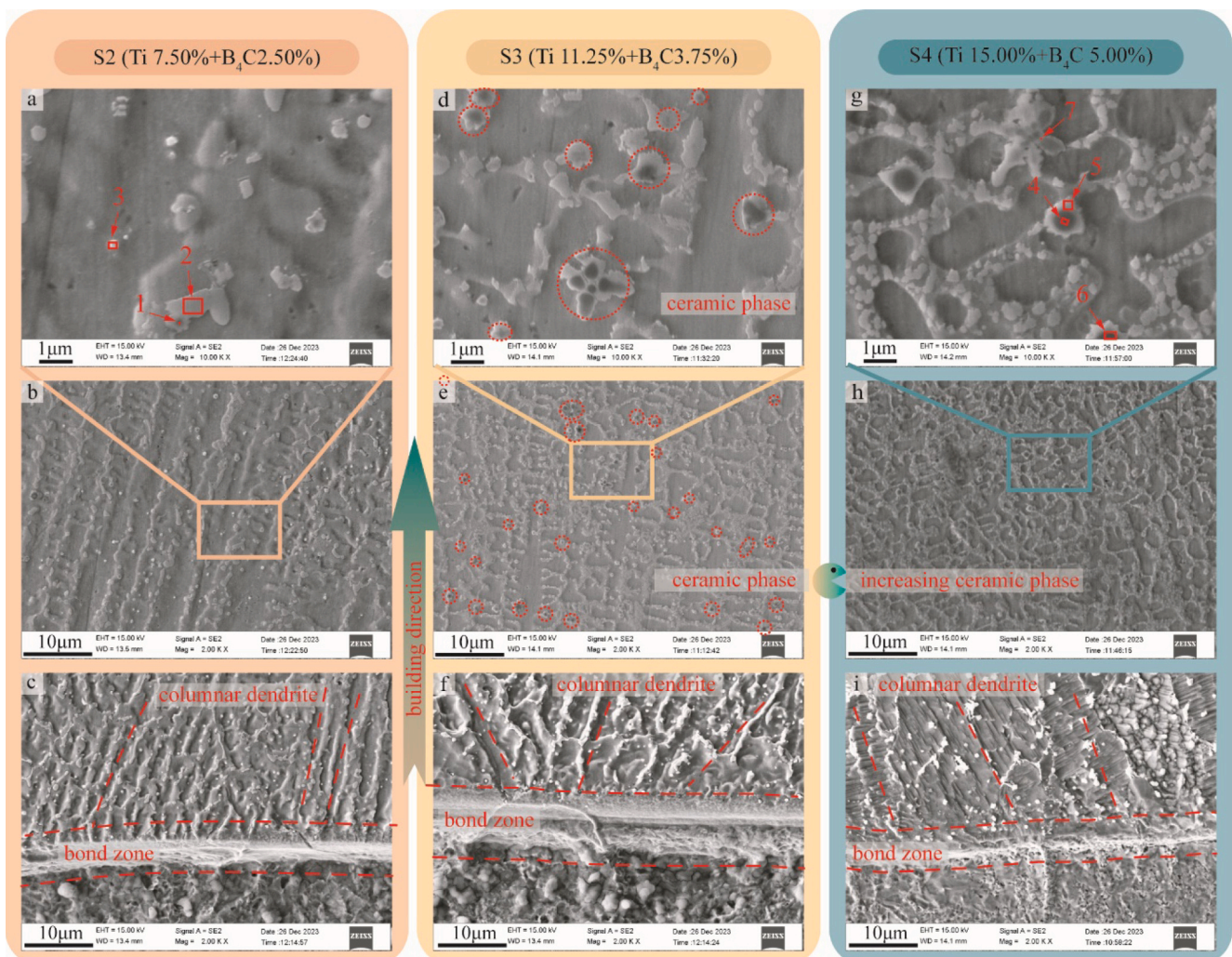


Fig. 11. SEM micrographs of samples and corresponding points distribution of EDS.

Table 3
Elemental composition (at.%) of the phases in samples S2 and S4.

	Area	B	C	Al	Ti	Cr	Fe	Ni	Nb	Mo	Possible phase
S2	1	6.88	38.29	1.01	11.91	8.79	8.46	14.61	8.50	1.55	TiB ₂ (Ti, Nb)C
	2	15.72	28.25	0.45	5.67	8.80	13.13	19.09	7.32	1.57	TiB ₂ (Ti, Nb)C
	3	35.23	16.68	0.39	3.43	8.04	12.43	21.71	1.37	0.72	Cr ₃ B ₂
	4	0	29.40	5.27	34.13	6.49	9.36	8.18	6.08	1.09	TiC (Ti, Nb)C
S4	5	32.29	29.27	1.90	17.45	4.03	5.06	5.16	4.10	0.73	TiB ₂
	6	24.87	22.87	6.23	29.58	3.14	4.11	3.85	4.81	0.55	TiB ₂ TiC (Ti,Nb)C
	7	0	37.11	0.48	9.17	9.49	18.06	21.29	3.47	0.93	(Ti, Nb)C

showed that TiB₂ and TiC have a 1.6 % lattice mismatch, which is far below the critical value of forming coherent lattice interfaces (16 %). Therefore, a cohesive relationship with reduced interfacial energy can be formed between the TiB₂ and TiC lattices, resulting in strong bonding at the coherent interface. C and B elements in TiB₂ and TiC ceramic

phases come from the decomposition of B₄C, promoting the adjacency proximity of these phases. The morphology of the phases at point 6 is similar to those at point 4 and point 5, indicating the synthesis of TiB₂, TiC, and (Ti, Nb)C phases. A gray-white long strip block at point 7 is rich in C, Ti, and Nb, indicating the synthesis of the (Ti, Nb)C phase. In

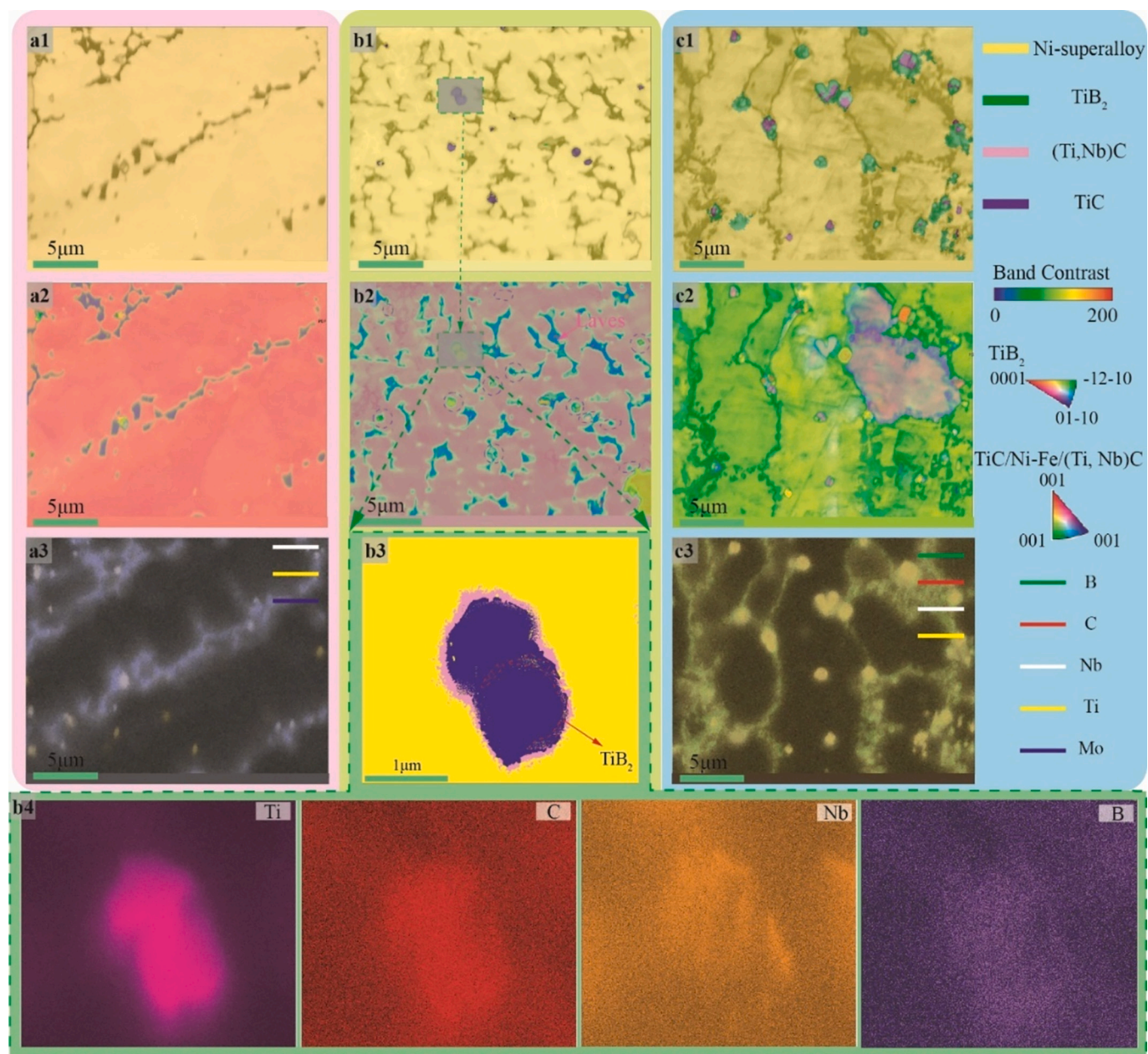


Fig. 12. The EBSD mapping in sample S0, sample S3, and sample S4: (a1, b1, and c1) Band contrast + phase mappings of the sample S1, sample S2, and sample S3; (a2, b2, c2) IPF + band contrast mappings along the building direction; (a3 and c3) EDS mapping of sample S0 and S4; (b3) Magnified mapping of ceramic phase of sample S3; and (b4) EDS mapping of the main elements correspond with figure b3.

summary, TiB₂, TiC, and (Ti, Nb)C phases tended to co-exist in the coatings.

In Fig. 11(d, g), in-situ synthesized ceramic phases are distributed at grain boundaries. Furthermore, several fine phases are synthesized at the grain boundaries (Fig. 11g). As the sizes of these phases decrease, the B₄C + Ti content increases and grain boundaries become rough (see Fig. 11a, d, g). These preferentially in-situ synthesized ceramic phases facilitate the nucleation rate, inhibiting the growth of other grains [40]. So, the phases in the grain boundaries are fine.

To further elucidate the synthesis and evolution of the ceramic phase, the EBSD analysis was performed on sample S0, sample S3, and sample S4, respectively. Fig. 12 (a1, b1, and c1) shows the BC + Ph (band contrast + phase) mappings of the coatings along the building direction. In Inconel 718 coating, the main phase is γ phase. As the B₄C + Ti content is added, the ceramic phases TiC, TiB₂, and (Ti, Nb)C are in-situ synthesized, and the ceramic phases increase with the addition of the B₄C + Ti content. The B, C, Nb, and Ti elements of sample S4 are superposed in Fig. 12 c3 EDS mapping. As evident in Fig. 12 (b1, c1, b3, c3), the position relations of in-situ synthesized ceramic phases are revealed. The loop (Ti, Nb)C phase encapsulates the TiC phase and TiB₂ phase; The TiC phase is distributed in the center, while the TiB₂ phase is distributed on the periphery. In sample S3, the TiB₂ phase is small in size and small in quantity, so it is not obvious. Because the B element easily reacts with air during laser DED. Furthermore, the EDS mapping of Ti, Nb, C, and B elements, which is shown in Fig. 12 (b4), also confirms the TiB₂ phase. However, in sample S4, the TiB₂ is obvious, and the TiB₂ is around the TiC phase. Fig. 12 (c3) also confirms this conclusion. Some long strip-like phases are found in Fig. 12 a2 and b2. The long strip-like phases are directional with the building direction but non-directional in sample S3. When the B₄C + Ti content increases, the long strip-like phase is few. Fig. 12 a3 shows the EDS mapping, which superposes the Ti, Nb, and Mo elements of sample S0. The long strip-like phases are rich in the Nb-Mo-Ti-Fe-Ni-Cr elements. Therefore, these phases are identified as the Laves phase, which is consistent with previous studies [41–43]. Notably, the in-situ ceramic phase, which grows on the Laves phase, exists in a circle or small block morphology.

According to the reaction order in Fig. 7 and the results of SEM and EBSD, the schematic illustration of microstructure evolution is clearly visible in Fig. 13. It is worth noting that the beginning synthesized time of γ phase is before the Cr₂₃C₆ phase and Cr₃B₂, even though the G value of γ phase is more than the G value of Cr₂₃C₆ phase and Cr₃B₂ phase (Fig. 7). In view of the fact that the synthesized temperature of γ phase is higher than Cr₂₃C₆ phase and Cr₃B₂ phase. So, during the solidification,

the γ phase reaches the synthesized condition first. However, the change of solidification temperature is significantly fast, so it is considered that the Cr₂₃C₆ phase and Cr₃B₂ phase begin to solidify during the solidification of the γ phase.

3.4. Mechanical properties

3.4.1. Microhardness

Fig. 14 (a) indicates the microhardness distribution of the coatings along the building direction. Three points are selected on the same horizontal line to obtain the average microhardness. Fig. 14(b) displays the morphology of the indentations. It indicates that the coatings maintain good toughness, which is consistent with previous research [44]. Fig. 14(c) illustrates the variation trend of the microhardness, which has a significant increase from sample S0 to S4. The average microhardness under the steady-state condition is shown in Fig. 14(d). The microhardness increases from 240.70 HV to 447.30 HV. The average microhardness of the S1 coating is 304.95 HV, which is enhanced by 11.10 % compared with sample S0. The S4 coating has the highest microhardness (447.30 HV), which is 1.86 and 1.63 times higher than the substrate and sample S0 coating, respectively. The microhardness of the coating is proportional to the B₄C + Ti content, as described by the following equation:

$$H = 473.84 - 200.14 / \left(1 + (X/9.99)^{2.30} \right) \quad (6)$$

Where H is microhardness. The R-squared is 0.9933. The increase in microhardness is attributed to the in-situ ceramic phase. In this reinforced process, the in-situ synthesized reinforced phases play multiple roles. Firstly, the nucleation sites are created by the synthesized ceramic phases, which promote crystallization. Secondly, the grain structure is refined by the synthesized ceramic phase, which improves mechanical properties [45]. Therefore, the coatings enhance deformation resistance through fine reinforcements.

The microhardness of all the samples in the heat-affected zone (HAZ) has significantly increased, which is attributed to the treatment of continuous laser energy input during the laser DED process. The fine and hard martensitic structure is formed in the HAZ. The microhardness variations on the HAZ of sample S4 were studied along the building direction (see Fig. 14e). Fig. 14(j) illustrates that microhardness in the HAZ generally decreases from the top zone (adjacent to the bond zone) to the substrate. The significant microhardness change is in the region between the top zone and the bond zone, which indicates the

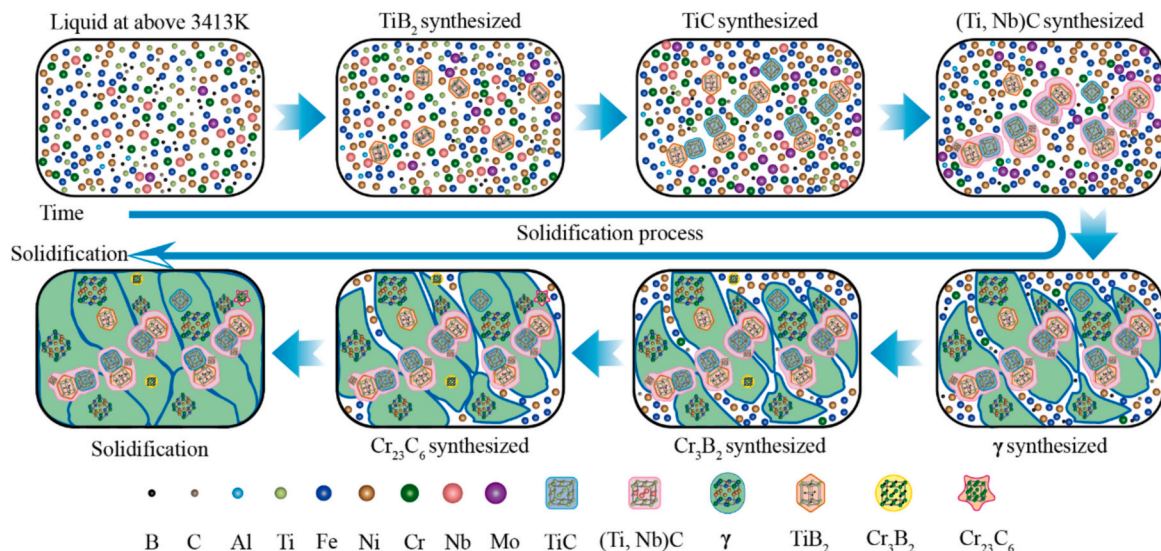


Fig. 13. The schematic illustration of microstructure evolution in sample S3.

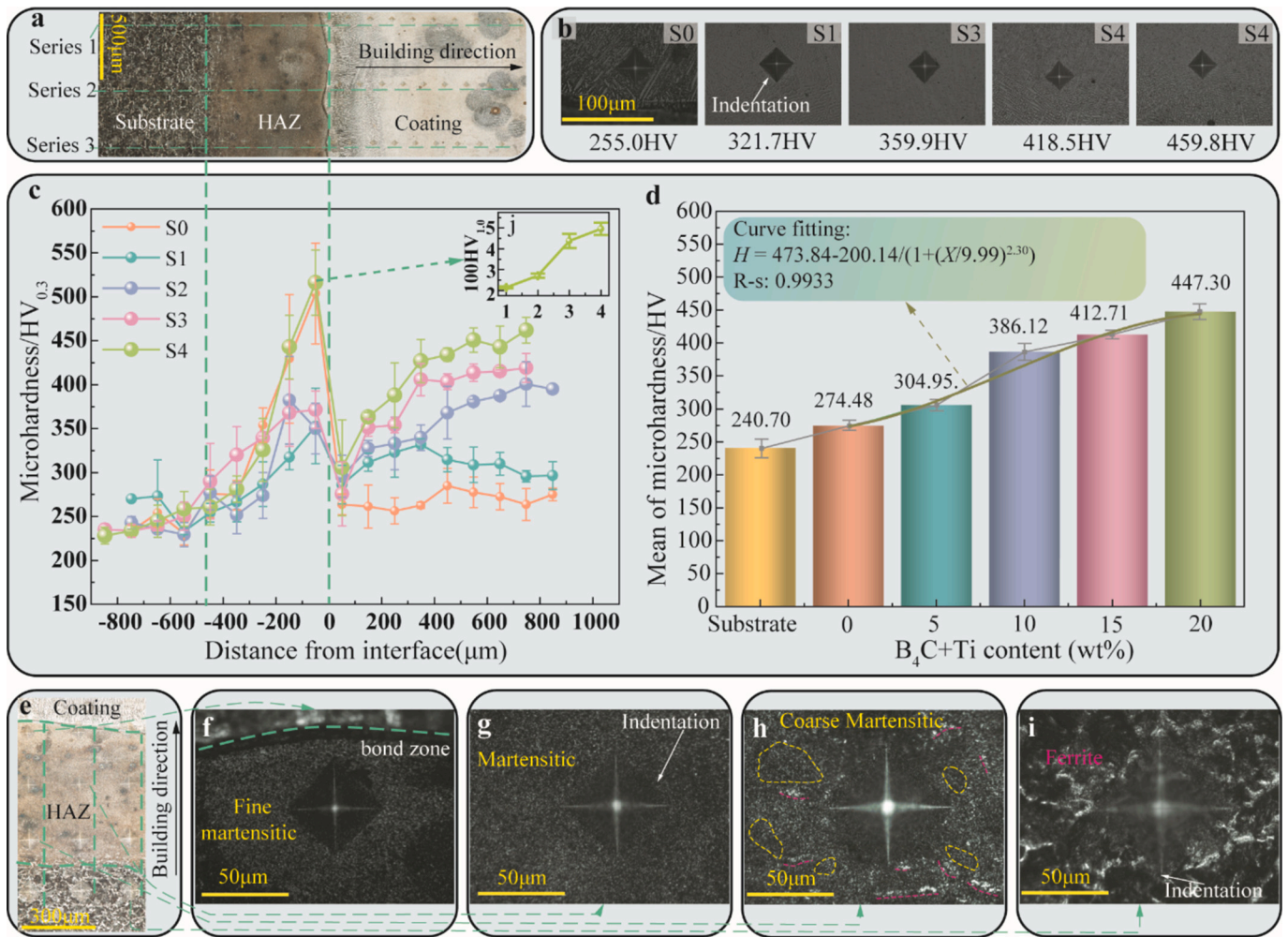


Fig. 14. (a) Microhardness indentation distribution; (b) The morphology of the typical indentations; (c) Microhardness trend of the samples; (d) The average value of the microhardness; (e) Microhardness indentation distribution in the HAZ; and (f-i) Typical indentations and optical microstructures in HAZ.

considerable changes in crystal structure during the laser DED process. The potential reason could be inferred that the higher temperature gradient of the substrate is caused by efficient heat dissipation. The high temperatures and temperature gradients at the HAZ-top zone can promote recrystallization and grain refinement. In addition, the top zone, which has the maximum number of elements (C, B, Ti, and Cr), has been exchanged with Inconel 718. These elements enhance the nucleation and grain refinement, thereby forming fine needle-martensite [46] (see Fig. 14f). These reasons explain why the top zone has the maximum microhardness in the HAZ. The HAZ-mid zone has slightly coarser grains (see Fig. 14g) due to the lower temperature gradient and slower nucleation rates. Therefore, as the temperature decreases, the HAZ-bottom zone exhibits coarser martensitic and ferrite (Fig. 14 h).

3.4.2. Scratch performance

Fig. 15 shows the coefficient of friction (COF) and its magnified views (initial stage). This experiment attempts to select regions that avoid pores and cracks. At the initial stage, the COF of samples S0 and S1 rapidly increased, then briefly stabilized before increasing again. When it reaches a threshold, the COF is finally stabilized. The reason for the abrupt increase in COF is the big resistance of plastic flow during the initial scratch stage [47]. Moreover, the COF enters a stable stage after the fluctuation stage, which indicates shear deformation has occurred. Samples S3 and S4 have a steady COF growth trend, indicating that material toughness is decreasing.

Optical and localized magnified views of the scratches are exhibited

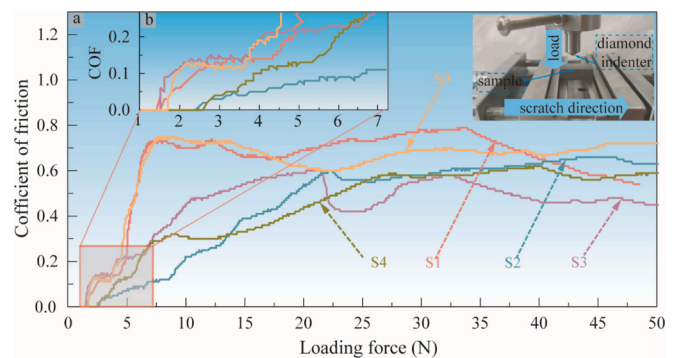


Fig. 15. Effect of the loading force on the COF: (a) The curves of COF versus applied load, (b) the magnified view of the friction coefficient at the initial stage.

in Fig. 16, which illustrate the different scratch mechanisms associated with the COF. Grooves can be seen in Fig. 16(a2-b2, a6-b6) at the initial scratch stage, indicating the generation of shear deformation. The smaller grooves can be found at the initial scratch stage of samples S3 and S4 (Fig. 16c2, d2, c6, d6). It indicates that plastic deformation and fracture could still occur under minimal loading conditions. The scratch length decreased by 38.94%, from 1493.33 μm to 911.82 μm. It reveals that the coating resistance to deformation has increased. It also

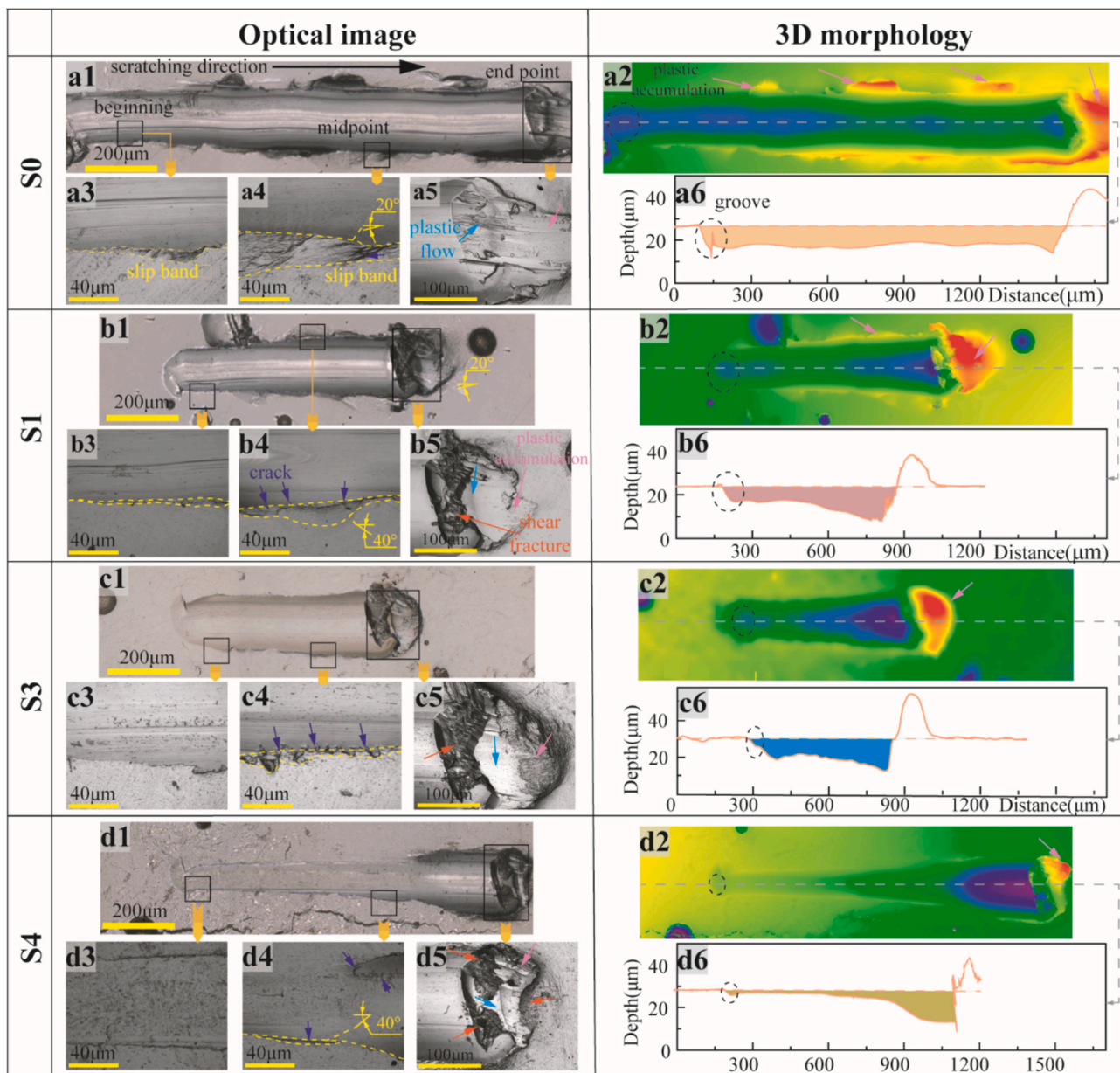


Fig. 16. (a1–d1) Scratch morphology of samples; (a2–d2) The image height of scratch morphology; (a3–d3) The localized magnified views of the beginning point of the scratches; (a4–d4) The localized magnified views of the midpoint of the scratches; (a5–d5) The localized magnified views of the endpoint of the scratches; and (a6–d6) The central sections of scratches along the depth direction.

indirectly suggests that the toughness of the coating decreases. The scratch morphology showed a significant change between samples S0 and S1, which indicated that the addition of $B_4C + Ti$ powder promotes surface modification. The plastic accumulation occurred at the scratch edges and decreased as the $B_4C + Ti$ content increased. It indicates that the deformation resistance has increased and plastic deformation has decreased. The beginning, midpoint, and endpoint of the scratch are marked in Fig. 16 (a3–d3, a4–d4, a5–d5), respectively. For sample S0, due to the metal plow, the plastic deformation may be the main removal mechanism during the scratch test. However, the slip bandwidth of sample S1 is significantly decreased. The slip band of sample S4 is the smallest. The cracks could be found in sample S1 (Fig. 16 b4). Firstly, plastic deformation occurs due to good plasticity, which prevents the generation of cracks in the slip bands. Subsequently, as the loading force increases, the plastic deformation intensifies. The cracks occur in the slip bands when the tensile stress exceeds the bonding strength. The numbers and volumes of these cracks increased with increasing $B_4C + Ti$

content. The direction of these crack propagation is parallel to the direction of the metal flow. The angle between metal flow and slip direction increases from 20° to 40° (Fig. 16 a4, b4, c4, and d4). Moreover, the plastic accumulation at the scratch endpoint gradually decreases. The shear fractures can be observed at the end of sample S1 scratch, and the fracture area increases as the $B_4C + Ti$ content increases.

The ceramic phases are mainly bound by weak ionic or covalent bonds, making them susceptible to fracture under stress. The ceramic phases hardly undergo plastic deformation, so they usually break directly after the elastic deformation stage. Conversely, due to the strong metallic bonds which are non-directional and have high plasticity, the metal undergoes plastic deformation after the elastic deformation stage. Because the yield strength of the Inconel 718 matrix exceeds that of ceramic phases, elasticity modulus is a mathematical description of the tendency of an object to deform when subjected to an external force [48]. Therefore, sample S0 has the widest slip band, the longest plastic slip band, and the smallest plastic flow angle (20°) at the same location.

Due to the higher elastic modulus of ceramic phases compared to the Inconel 718 matrix, the deformation of in-situ synthesized ceramic phases is less than that of the Inconel 718 matrix.

The cracks form and propagate towards the edges as the tensile stress increases. The strain at the ceramic phase edges increases as the numbers and size of ceramic phases increase, which promotes the generation and propagation of cracks. When the crack propagated to the surface, it started to fall off. Therefore, when the reinforcements are in-situ synthesized, plastic accumulation at the end of the scratch decreases, and shear fracture begins to occur. Because the microhardness of ceramic phases exceeds that of the Inconel 718 matrix, the metal matrix undergoes plastic deformation. When the dislocation and deformation within the coating spread to the high-hardness ceramic phases, the Orowan effect occurs [49]. Therefore, as the size and volume fraction of the synthesized phases increase, so does their deformation resistance, resulting in a gradual decrease in scratch depth (see Fig. 16 (a6-d6)).

3.4.3. Wear resistance

According to the COF variation curve (see Fig. 17), the two stages can be used to observe the wear process: sharp wear and stable wear. As shown in Fig. 17(b), during the sharp wear stage, the contact area of the friction pairs (Al_2O_3 grinding ball and coatings) is small, limiting the material removal. However, as the grinding balls gradually wear, the surface material bulges and falls off, causing significant fluctuations in COF. Meanwhile, the friction force fluctuates significantly due to the variation in surface roughness, leading to a rapid increase in the COF [50]. As more material is removed under the larger loading force, the wear process enters a stable stage (Fig. 17c). In this stage, the high-hardness reinforcing phases act as a “skeleton”, which effectively prevents the micro-cutting process of the softer matrix. It can be attributed to the fact that these reinforcing phases sustain more contact stress, and reduce the contact area between friction pairs. The ceramic reinforcing phases reduce the material removal and enhance friction stability. The COF average value of samples can be identified from Fig. 19 (a). Sample S0 has the highest COF value. The COF decreases linearly with increasing $\text{B}_4\text{C} + \text{Ti}$ content, with a minimum value of 0.5393 (Sample S4). It can be expressed as follows:

$$C = 0.52 + 0.10 / \left(1 + (X/9.59)^{2.12} \right) \quad (7)$$

Where C is the COF value. The R-squared is 0.9943. The COF of sample S4 is only 0.87 times that of S0. The average COF indicates that adding $\text{B}_4\text{C} + \text{Ti}$ powder at room temperature can significantly improve the lubrication of the coatings.

The wear mass, which is measured by the electronic balance, decreases from 2.19 mg (Sample S0) to 1.19 mg (Sample S3), reduced by 45.66 % (see Fig. 18 b). The wear mass of Sample S4 has increased to 1.82 mg. The wear rate (R) can be calculated using Eq. (6) [51]:

$$R = \frac{V_m}{N \times S} \quad (8)$$

Where N is the loading force (15 N), S is the wear distance, and V_m is the wear volume. The value of wear rate (samples S0-S3) decreases by 79.44 %, from $8.27 \times 10^{-4} \text{ mm}^3/\text{Nm}$ to $1.70 \times 10^{-4} \text{ mm}^3/\text{Nm}$. A turning point appears in sample S3. During the wear process, the properties of the ceramic phases (size, composition, proportion, and bonding strength with the matrix) have a significant influence on the wear rate [37]. Sample S0 has the lowest microhardness, so it has the highest wear volume. It is consistent with the law of Archard [52,53], which the microhardness of a material is proportional to its wear resistance. The material that has high hardness can prevent plastic deformation, inhibit crack generation, and reduce surface material removal. This study [52] indicated that significant residual stresses often exist within laser DED coatings, with their distribution being highly localized. The localized residual stress promotes the flaking of material from the wear surface of the coating. The debris that adhered to the grinding ball increased the friction resistance, resulting in higher COF values and wear rates. The wear rate of sample S4 has increased slightly. When the $\text{B}_4\text{C} + \text{Ti}$ addition ratio reaches 20 %, the distinctions between the ceramic phase and the matrix become more apparent because of their different physical parameters. Since the ceramic phases are small ($< 2.0 \mu\text{m}$) or even smaller than the micro-cutting plane, they are “dug out” with the matrix during the wear process. Zum et al. [54] also reported that when the carbides are smaller than $1.0 \mu\text{m}$, the wear resistance decreases with increasing carbide content. The ceramic phases have a negative impact on the wear resistance of sample S4. Fig. 18 (d) shows the cross-sectional profile of wear morphology. The wider and

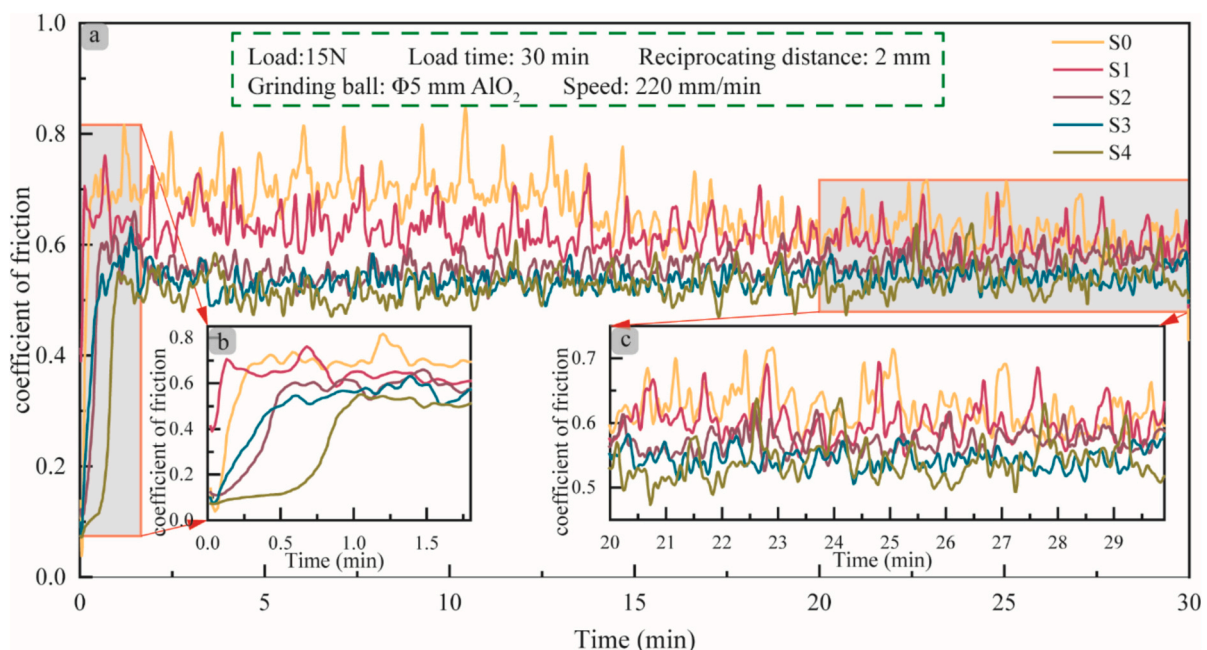


Fig. 17. (a). Time-dependent COF curves of different coatings, (b) COF at sharp wear stage, and (c) COF at stable wear stage.

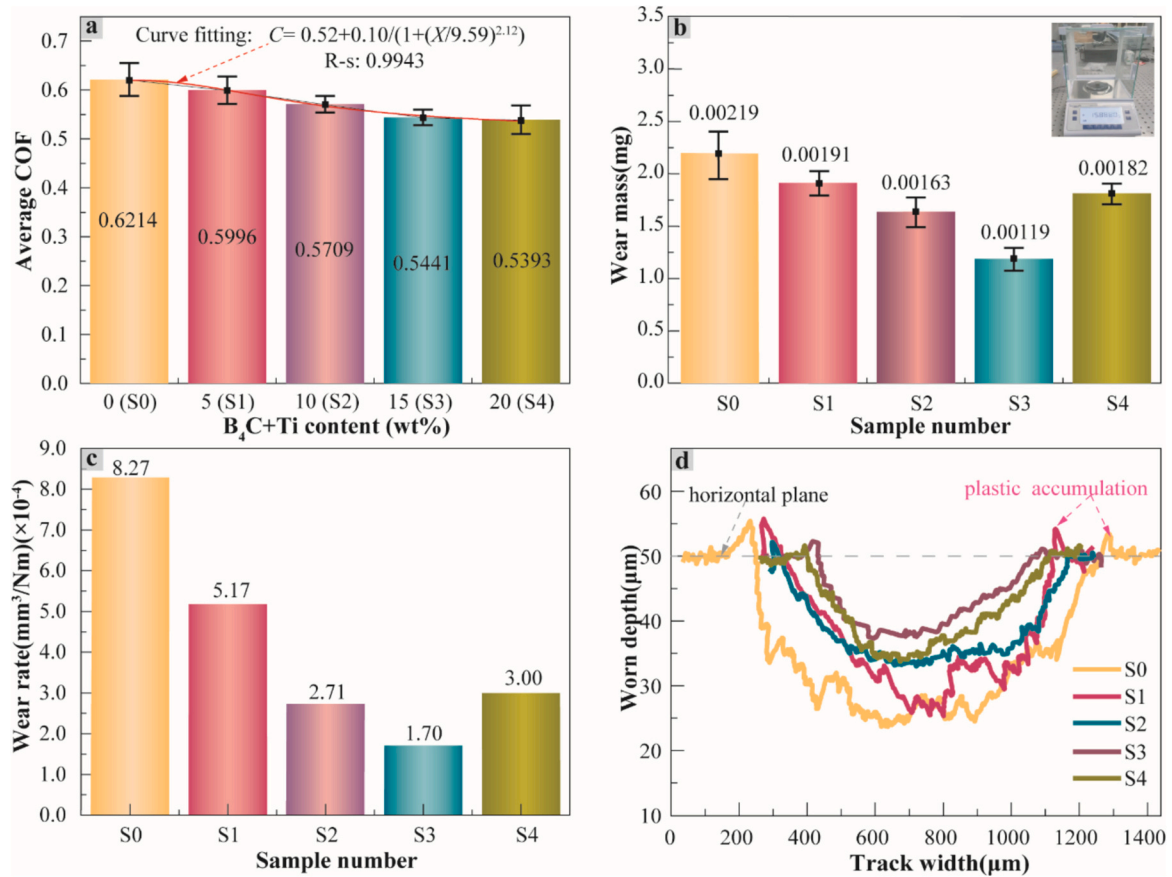


Fig. 18. (a) average COF of samples, (b) wear mass of samples, (c) wear rate of different samples, and (d) cross-sectional of scratch morphology from samples.

deeper wear scratches can be found in samples S0 and S1 due to the lower microhardness. Significant plastic accumulation at the wear edges indicates that samples S0 and S1 have relatively high toughness.

The wear surface becomes smoother and the track becomes smaller

with an increase of Ti and B₄C content. Fig. 19 shows optical images, 3D morphology, and top profiles of the Al₂O₃ grinding ball after the wear process. The top surface area of the grinding ball decreases from 774,669.50 μm² to 176,234.30 μm², reduced by 77.25 %. Fig. 19

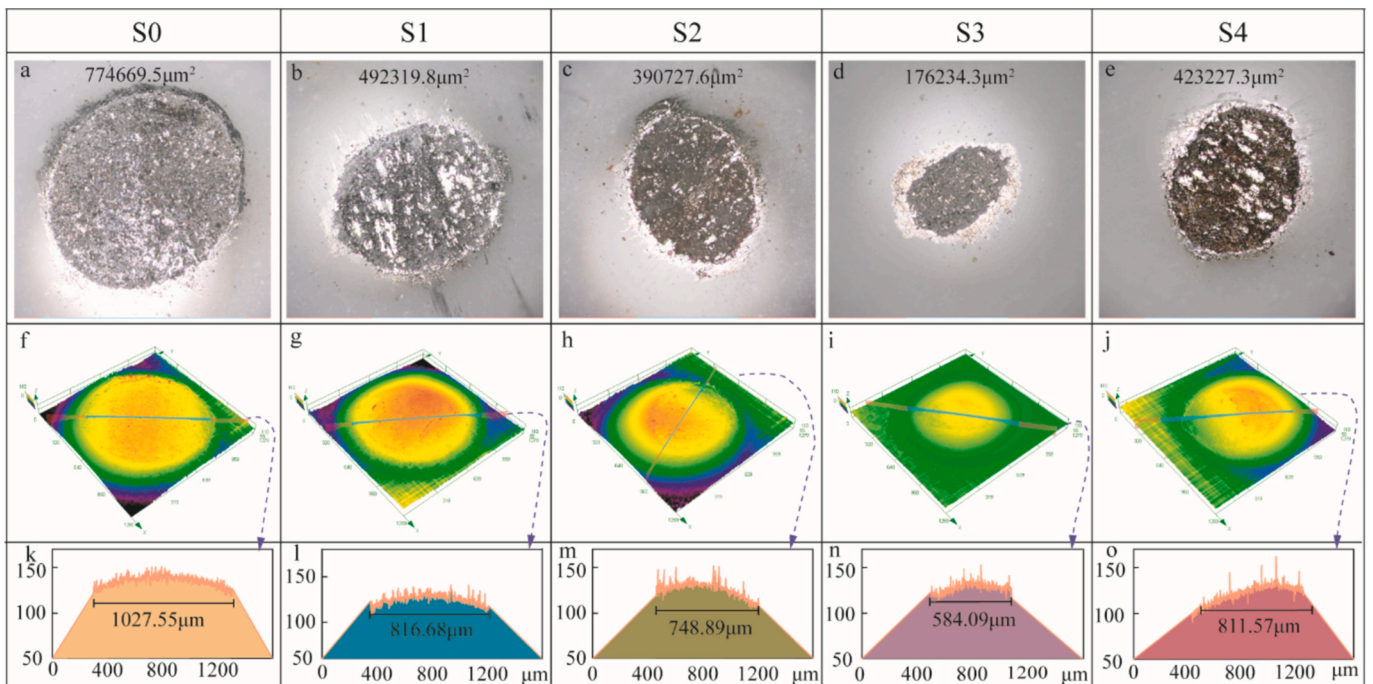


Fig. 19. (a-e) optical morphology of grinding balls, (f-j) 3D morphology of grinding balls, and (k-o) top profile of grinding balls.

illustrates sharp scratches on the grinding ball caused by the relative motion of the samples, intensifying up to sample S2.

To elucidate the relationship among COF, wear rate, and wear mechanism, the 2D and 3D surface morphology and line profiles of samples S0-S4 are demonstrated in Fig. 20. To unify research variables, the region without pores and cracks was selected as much as possible to test. Little cracks can be found on all worn surfaces. Fig. 20 (a, b, c) depicts a large area of material flake that may cause surface unevenness. The cross-sectional profiles are presented in Fig. 20(d, h, l, p, t). The height difference and standard deviation of the sectional profile along the building direction are measured (see Fig. 20 u). As the $B_4C + Ti$ content increases, the wear width decreases. Sample S0 has the largest wear width (1143.77 μm), which is 1.6 times greater than sample S4. The wear surface becomes smoother. Samples S0 and S1 exhibit poor surface flatness due to large flakes of worn surface. In contrast, the wear surfaces of samples S3 and S4 are smooth, which can be attributed to the change in the wear mechanism. This phenomenon also explains why samples S0-S1 have a high COF value, and the sample S2-S4 have a relatively stable COF value. Usually, during the reciprocating friction test, the sample surface is subjected to localized high-contact stress from the friction pair, which increases crack sensitivity and leads to crack initiation [55]. The flake-like pits are formed because of the crack propagation. The wear debris easily adheres to the grinding ball, which exhibits typical adhesive wear properties, as shown in sample S0. In sample S1, adhesive wear remains the dominant wear style, but continuous grooves along the wear direction begin to appear. The abrasive wear is observed in samples S2-S4, and two characteristics can be found: one is the small debris caused by localized material fall off, and the other is the long fracture grooves caused by abrasive scratches (see Fig. 20j, k, n, o). Specifically, the wear surface of sample S4 is very smooth, which only has grooves without large spalling pits. These phenomena indicate that the addition of $B_4C + Ti$ improves its lubrication and changes the wear mechanism. Ceramic phases reduce the fall-off of the low-hardness matrix and cause a lower wear rate. On the other

hand, the ceramic phases which are removed by micro-cutting provide lubrication during wear. Therefore, the ceramic phases reduce the value of COF and enhance surface smoothness [38].

4. Conclusions

In this paper, laser-directed energy deposition (DED) is utilized to in-situ synthesize TiB_2 , TiC , and $(Ti, Nb)C$ ceramic phases. The effect of five different Ti and B_4C contents on phase, microstructure, microhardness, scratch, and wear resistance was investigated. The impact of these ceramic phases on microstructure, porosity, thermodynamic analysis, microhardness, scratch performance, and wear resistance was thoroughly investigated. The main conclusions are as follows:

1. The addition of Ti + B_4C powder can increase the porosity. The relationship between the porosity and powder content was fitted. Thermodynamic analysis has been used to analyze the in-situ synthesized ceramic phases and reaction sequences ($TiB_2 > MC > Cr_3B_2 > Cr_{23}C_6$). Ti atoms can be substituted with Nb atoms, which can be represented as NbC , $(Ti_{0.25}Nb_{0.75})C$, $(Ti_{0.5}Nb_{0.5})C$, $(Ti_{0.75}Nb_{0.25})C$, and TiC . Ti atom and Nb atom, which have different distributions and ratios in MC (refer to TiC and $(Ti, Nb)C$) crystal structure, affect the Gibbs free energy (G). Conversely, the G values of the TiB_2 phase in different samples are consistent.
2. TiB_2 , TiC , and $(Ti, Nb)C$ ceramic phases don't like to exist separately before synthesizing synchronously. The positional relations of in-situ ceramic phases are as follows: The loop $(Ti, Nb)C$ phase encapsulated the TiC phase and TiB_2 phase; the TiC phase is distributed in the center, while the TiB_2 phase is distributed on the periphery. The in-situ ceramic phases are priorly synthesized on the laves phase or grain boundaries. The ceramic phases refine grain by increasing the nucleation rate, inhibiting the growth of other grains, and subsequently forming grain boundaries.

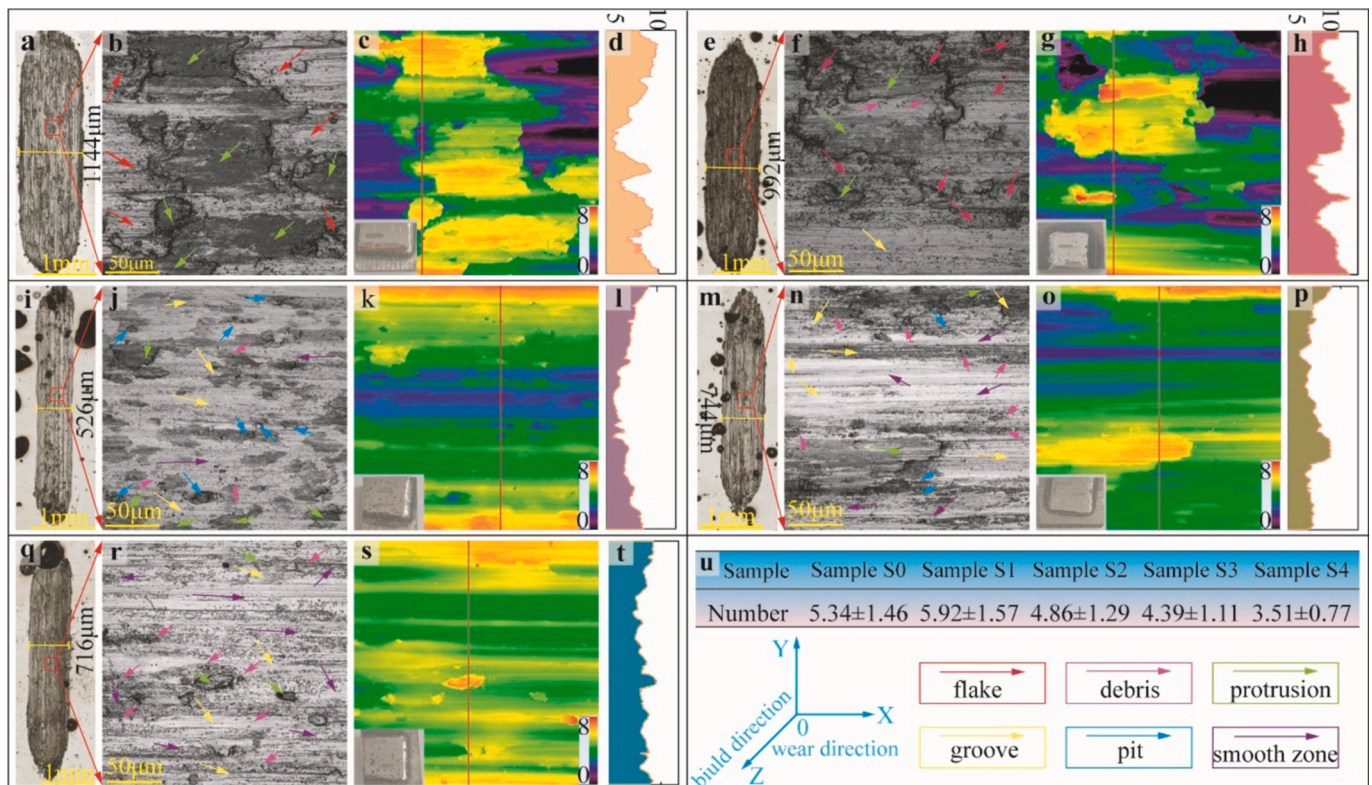


Fig. 20. Optical images of worn surfaces (a-d) sample S0, (e-h) sample S1, (i-l) sample S2, (m-p) sample S3, and (q-t) sample S4.

- As the B₄C + Ti content changes, the microhardness of the coatings increases from 274.48HV_{0.3} to 447.30HV_{0.3}. This increase results from in-situ synthesized ceramic phases, solid solution strengthening, and fine-grain strengthening. From the top zone to the substrate, microhardness in HAZ decreases by 56.74 %, from 495.95 HV to 215.07 HV. The rapid increase in HAZ microhardness is due to martensitic transformation, exchanged elements (C, B, Ti, and Cr), and HAZ temperature gradients.
- As B₄C + Ti content increases, the scratch length is decreased from 1493.330 μm to 911.822 μm, reduced by 38.94 %. The angle of the plastic flow increases from 20° to 40°, and the number and size of cracks in the plastic flow increase. The above phenomenon shows that the coatings increase deformation resistance but reduce toughness. The scratch deformation transforms from plastic deformation to shear fracture. Under increased loading force, the metal matrix in coatings first undergoes plastic deformation to resist loading force; when the dislocation is transmitted to ceramic phases, the Orowan effect occurs, which increases the resistance to external deformation.
- The wear resistance of the coatings has been significantly improved. The relationship between the COF and powder content is fitted. The coating with 11.25 % Ti powder and 3.75 % B₄C powder demonstrates the best wear resistance, exhibiting a 45.66 % reduction in wear mass and a 79.44 % reduction in wear rate compared to the Inconel 718 superalloy coating. As the B₄C + Ti powder content increases, the wear mechanism of the samples changes from adhesive wear to abrasive wear, and the lubrication of the coating is improved.

CRedit authorship contribution statement

Chuang Guan: Writing – review & editing, Writing – original draft, Methodology, Conceptualization. **Ying Chen:** Writing – review & editing, Investigation. **Fanwei Meng:** Investigation, Data curation. **Liaoyuan Chen:** Writing – review & editing, Supervision. **Zhelun Ma:** Resources, Methodology. **Tianbiao Yu:** Supervision, Resources, Funding acquisition.

Declaration of competing interest

We declare that we have no financial and personal relationships with other people or organizations that can inappropriately influence our work. There is no professional or other personal interest of any nature or kind in any product, service and/or company that could be construed as influencing the position presented in, or the review of. The manuscript entitled, “Microstructure and mechanical properties of in-situ TiB₂/TiC/(Ti, Nb)C reinforced Inconel 718 coating by laser direct energy deposition”.

Acknowledgment

This work was supported by the National Natural Science Foundation of China [Grant number 52075088], the Fundamental Research Funds for the Central Universities [N2303003].

Data availability

Data will be made available on request.

References

- Z. Yang, L. Zhu, S. Wang, J. Ning, Y. Dun, G. Meng, P. Xue, P. Xu, B. Xin, Effects of ultrasound on multilayer forming mechanism of Inconel 718 in directed energy deposition, *Addit. Manuf.* 48 (2021) 102462, <https://doi.org/10.1016/j.addma.2021.102462>.
- V.K. Singh, D. Sahoo, M. Amirthalangam, S. Karagadde, S.K. Mishra, Dissolution of the laves phase and δ-precipitate formation mechanism in additively manufactured Inconel 718 during post printing heat treatments, *Addit. Manuf.* 81 (2024) 104021, <https://doi.org/10.1016/j.addma.2024.104021>.
- Z. Yang, L. Zhu, J. Ning, S. Wang, P. Xue, P. Xu, Y. Dun, B. Xin, G. Zhang, Revealing the influence of ultrasound/heat treatment on microstructure evolution and tensile failure behavior in 3D-printing of Inconel 718, *J. Mater. Process. Technol.* 305 (2022) 117574, <https://doi.org/10.1016/j.jmatprotec.2022.117574>.
- A. Ghidini, S. Cantini, D. Petta, Optimised choices for safe and environmentally-friendly heat treatments of railway solid wheels, *Metall. Ital.* 114 (2022) 26–35.
- T.S. Liu, P. Chen, F. Qiu, H.Y. Yang, N.T.Y. Jin, Y. Chew, D. Wang, R. Li, Q.C. Jiang, C. Tan, Review on laser directed energy deposited aluminum alloys, *Int. J. Extrem. Manuf.* 6 (2024), <https://doi.org/10.1088/2631-7990/ad16bb>.
- L. Gao, A.C. Chuang, P. Kenesei, Z. Ren, L. Balderson, T. Sun, An operando synchrotron study on the effect of wire melting state on solidification microstructures of Inconel 718 in wire-laser directed energy deposition, *Int. J. Mach. Tools Manuf.* 194 (2024) 104089, <https://doi.org/10.1016/j.ijmactools.2023.104089>.
- Y. Zheng, F. Liu, W. Zhang, F. Liu, C. Huang, The microstructure evolution and precipitation behavior of TiB₂ / Inconel 718 composites manufactured by selective laser melting, *J. Manuf. Process.* 79 (2022) 510–519, <https://doi.org/10.1016/j.jmapro.2022.04.070>.
- J. Ning, Q. Lan, L. Zhu, L. Xu, Z. Yang, P. Xu, P. Xue, B. Xin, Microstructure and mechanical properties of SiC-reinforced Inconel 718 composites fabricated by laser cladding, *Surf. Coat. Technol.* 463 (2023) 129514, <https://doi.org/10.1016/j.surfcoat.2023.129514>.
- S. Bhatnagar, S. Mullick, A study on the influence of reinforcement particle size in laser cladding of TiC / Inconel 625 metal matrix composite, *Opt. Laser Technol.* 161 (2023) 109115, <https://doi.org/10.1016/j.optlastec.2023.109115>.
- A. Teber, F. Schoenstein, F. Tétard, M. Abdellaoui, N. Jouini, Effect of SPS process sintering on the microstructure and mechanical properties of nanocrystalline TiC for tools application, *Int. J. Refract. Met. Hard Mater.* 30 (2012) 64–70, <https://doi.org/10.1016/j.ijrmhm.2011.06.013>.
- J. Song, C. Huang, M. Lv, B. Zou, S. Wang, J. Wang, J. An, Effects of TiC content and melt phase on microstructure and mechanical properties of ternary TiB₂-based ceramic cutting tool materials, *Mater. Sci. Eng. A* 605 (2014) 137–143, <https://doi.org/10.1016/j.msea.2014.03.036>.
- W. Cui, Y. Li, F. Li, X. Qi, X. Sun, Z. Pan, J. Niu, Wear and corrosion properties of in-situ TiC-TiB₂ modified Ni-based composite coatings with different B/C ratios prepared by laser cladding, *Ceram. Int.* 50 (2024) 2424–2435, <https://doi.org/10.1016/j.ceramint.2023.11.027>.
- B. Sie, C. Tjong, Novel nanoparticle-reinforced metal matrix composites with enhanced mechanical properties, *Adv. Eng. Mater.* (2007) 639–652, <https://doi.org/10.1002/adem.200700106>.
- Y. Pan, Y. Liu, F. Kuang, C. Lei, X. Lu, In-situ formed TiCx reinforced Ti composites derived from polyzirconocarbosilane precursor: synthesis, characterization and mechanical properties, *Mater. Charact.* 217 (2024), <https://doi.org/10.1016/j.matchar.2024.114365>.
- S. Moya, S. Lopez-esteban, C. Pecharrroma, The challenge of ceramic / metal microcomposites and nanocomposites, *Prog. Mater. Sci.* 52 (2007) 1017–1090, <https://doi.org/10.1016/j.pmatsci.2006.09.003>.
- Z. Wang, J. Li, Q. Liu, L. Chen, J. Lv, T. Yu, J. Zhao, No-impact trajectory design and fabrication of surface structured CBN grinding wheel by laser cladding remelting method, *Opt. Laser Technol.* 181 (2025), <https://doi.org/10.1016/j.optlastec.2024.111956>.
- J. Ye, J. Yang, X. Chen, H. Luo, J. Li, T. Chen, S. Zhou, F. Pan, Microstructure and tensile properties of in-situ TiAl nanoparticles reinforced AZ31 composites, *Mater. Charact.* 217 (2024), <https://doi.org/10.1016/j.matchar.2024.114381>.
- Y. Bin Cao, H.T. Ren, C.S. Hu, Q.X. Meng, Q. Liu, In-situ formation behavior of NbC-reinforced Fe-based laser cladding coatings, *Mater. Lett.* 147 (2015) 61–63, <https://doi.org/10.1016/j.matlet.2015.02.026>.
- L. Chen, Y. Chen, X. Chen, T. Yu, Z. Wang, Microstructure and properties of in situ TiC/Ni functionally gradient coatings by powder-fed laser cladding, *Ceram. Int.* (2022), <https://doi.org/10.1016/j.ceramint.2022.08.243>.
- W. Gao, Y. Zhou, X. Han, S. Li, Z. Huang, Preparation and microstructure of 3D framework TiC-TiB₂ ceramics and their reinforced steel matrix composites, *Ceram. Int.* 47 (2021) 2329–2337, <https://doi.org/10.1016/j.ceramint.2020.09.075>.
- C. Zhao, Y. Zhou, X. Xing, S. Liu, X. Ren, Q. Yang, Precipitation stability and micro-property of (Nb, Ti)C carbides in MMC coating, *J. Alloys Compd.* 763 (2018) 670–678, <https://doi.org/10.1016/j.jallcom.2018.05.318>.
- C. Zhou, S. Zhao, Y. Wang, F. Liu, W. Gao, X. Lin, Mitigation of pores generation at overlapping zone during laser cladding, *J. Mater. Process. Technol.* 216 (2015) 369–374, <https://doi.org/10.1016/j.jmatprotec.2014.09.025>.
- J. Karimi, C. Suryanarayana, I. Okulov, K.G. Prashanth, Selective laser melting of Ti6Al4V: effect of laser re-melting, *Mater. Sci. Eng. A* 805 (2021), <https://doi.org/10.1016/j.msea.2020.140558>.
- P. Xue, L. Zhu, J. Ning, P. Xu, S. Wang, Z. Yang, Y. Ren, G. Meng, The crystallographic texture and dependent mechanical properties of the CrCoNi medium-entropy alloy by laser remelting strategy, *J. Mater. Sci. Technol.* 111 (2022) 245–255, <https://doi.org/10.1016/j.jmst.2021.08.094>.
- J. Wang, J. Shen, Z. Shen, H. Qian, Q. Zhou, Z. Huang, Analysis of the crack initiation and short crack propagation of laser cladding IN718 enduring fretting fatigue at 650 °C, *Tribol. Int.* 194 (2024), <https://doi.org/10.1016/j.triboint.2024.109484>.
- M. Li, J. Zhang, T. Mi, C. Zheng, D. Wu, Z. Chen, X. Yi, Improvement mechanism of Mo element on cracks, microstructure and properties of laser cladding WC-Ni60AA coating, *Surf. Coat. Technol.* 489 (2024) 131047, <https://doi.org/10.1016/j.surfcoat.2024.131047>.

- [27] G. Ma, S. Zhu, D. Wang, P. Xue, B. Xiao, Z. Ma, Effect of heat treatment on the microstructure, mechanical properties and fracture behaviors of ultra-high-strength SiC/Al–Zn–Mg–Cu composites, *Int. J. Miner. Metall. Mater.* 31 (2024) 2233–2243, <https://doi.org/10.1007/s12613-024-2856-1>.
- [28] C. Lee, H. Park, J. Yoo, C. Lee, W. Woo, S. Park, Residual stress and crack initiation in laser clad composite layer with Co-based alloy and WC + NiCr, *Appl. Surf. Sci.* 345 (2015) 286–294, <https://doi.org/10.1016/j.apsusc.2015.03.168>.
- [29] Z. Tianyu, Thermodynamic analysis and mechanical properties of Nb-Si based alloy alloyed with C element, 2020, <https://doi.org/10.27061/d.cnki.ghgdu.2020.001585>.
- [30] W. Lu, Q. An, C. Wang, S. Wang, L. Huang, F. Sun, R. Chen, L. Geng, Sub-micron grains and excellent mechanical properties of low-density Ti40Nb30Mo30-C refractory complex concentrated alloy reinforced with in-situ (Ti, Nb)C, *Mater. Sci. Eng. A* 860 (2022) 144335, <https://doi.org/10.1016/j.msea.2022.144335>.
- [31] C. Guan, T. Yu, Y. Zhao, L. Chen, Y. Chen, Repair of gear by laser cladding Ni60 alloy powder: process, microstructure and mechanical performance, *Appl. Sci.* 13 (2023) 319, <https://doi.org/10.3390/app13010319>.
- [32] X. Ding, Y. Koizumi, D. Wei, A. Chiba, Effect of process parameters on melt pool geometry and microstructure development for electron beam melting of IN718: a systematic single bead analysis study, *Addit. Manuf.* 26 (2019) 215–226, <https://doi.org/10.1016/j.addma.2018.12.018>.
- [33] H.L. Wei, G.L. Knapp, T. Mukherjee, T. DebRoy, Three-dimensional grain growth during multi-layer printing of a nickel-based alloy Inconel 718, *Addit. Manuf.* 25 (2019) 448–459, <https://doi.org/10.1016/j.addma.2018.11.028>.
- [34] Z. Yang, L. Zhu, S. Wang, J. Ning, Y. Dun, G. Meng, P. Xue, P. Xu, B. Xin, Effects of ultrasound on multilayer forming mechanism of Inconel 718 in directed energy deposition, *Addit. Manuf.* 48 (2021) 102462, <https://doi.org/10.1016/j.addma.2021.102462>.
- [35] A. Teresiak, H. Kubsch, X-ray investigations of high energy ball milled transition metal carbides, *Nanostruct. Mater.* 6 (1995) 671–674, [https://doi.org/10.1016/0965-9773\(95\)00147-6](https://doi.org/10.1016/0965-9773(95)00147-6).
- [36] S. Lv, Y. Zu, G. Chen, X. Fu, W. Zhou, An ultra-high strength CrMoNbWTi-C high entropy alloy co-strengthened by dispersed refractory IM and UHTC phases, *J. Alloys Compd.* 788 (2019) 1256–1264, <https://doi.org/10.1016/j.jallcom.2019.02.318>.
- [37] L. Chen, Y. Zhao, F. Meng, T. Yu, Z. Ma, S. Qu, Z. Sun, Effect of TiC content on the microstructure and wear performance of in situ synthesized Ni-based composite coatings by laser direct energy deposition, *Surf. Coat. Technol.* 444 (2022) 128678, <https://doi.org/10.1016/j.surfcoat.2022.128678>.
- [38] Y. Zhao, T. Yu, L. Chen, Y. Chen, C. Guan, J. Sun, Microstructure and wear resistance behavior of Ti–C–B4C-reinforced composite coating, *Ceram. Int.* 46 (2020) 25136–25148, <https://doi.org/10.1016/j.ceramint.2020.06.300>.
- [39] M. Masanta, S.M. Shariff, A. Roy Choudhury, Evaluation of modulus of elasticity, nano-hardness and fracture toughness of TiB2-TiC-Al2O3 composite coating developed by SHS and laser cladding, *Mater. Sci. Eng. A* 528 (2011) 5327–5335, <https://doi.org/10.1016/j.msea.2011.03.057>.
- [40] L. Chen, T. Yu, P. Xu, B. Zhang, In-situ NbC reinforced Fe-based coating by laser cladding : simulation and experiment scanning direction coating, *Surf. Coat. Technol.* 412 (2021) 127027, <https://doi.org/10.1016/j.surfcoat.2021.127027>.
- [41] G.D.J. Ram, A.V. Reddy, K.P. Rao, G.M. Reddy, Control of laves phase in inconel 718 GTA welds with current pulsing, *Sci. Technol. Weld. Join.* 9 (2004) 390–398, <https://doi.org/10.1179/136217104225021788>.
- [42] S. Sui, J. Chen, E. Fan, H. Yang, X. Lin, W. Huang, The influence of laves phases on the high-cycle fatigue behavior of laser additive manufactured Inconel 718, *Mater. Sci. Eng. A* 695 (2017) 6–13, <https://doi.org/10.1016/j.msea.2017.03.098>.
- [43] Y. Zhang, Z. Li, P. Nie, Y. Wu, Effect of precipitation on the microhardness distribution of diode laser Epitaxially deposited IN718 alloy coating, *J. Mater. Sci. Technol.* 29 (2013) 349–352, <https://doi.org/10.1016/j.jmst.2013.01.002>.
- [44] D.T. Waghmare, C. Kumar Padhee, R. Prasad, M. Masanta, NiTi coating on Ti-6Al-4V alloy by TIG cladding process for improvement of wear resistance: microstructure evolution and mechanical performances, *J. Mater. Process. Technol.* 262 (2018) 551–561, <https://doi.org/10.1016/j.jmatprotec.2018.07.033>.
- [45] D. Tijo, M. Masanta, In-situ TiC-TiB2 coating on Ti-6Al-4V alloy by tungsten inert gas (TIG) cladding method: part-II. Mechanical performance, *Surf. Coat. Technol.* 344 (2018) 579–589, <https://doi.org/10.1016/j.surfcoat.2018.03.083>.
- [46] Z. Rui, L. Hongliang, T. Xingyin, Study on microstructure and mechanical properties of ultrafine-grained 45 steel, *Metall. Eng.* 01 (2014) 35–39, <https://doi.org/10.12677/meng.2014.12006>.
- [47] D.F.S. Ferreira, J.S. Vieira, S.P. Rodrigues, G. Miranda, F.J. Oliveira, J.M. Oliveira, Dry sliding wear and mechanical behaviour of selective laser melting processed 18Ni300 and H13 steels for moulds, *Wear* 488–489 (2022), <https://doi.org/10.1016/j.wear.2021.204179>.
- [48] Z. Ma, Q. Wang, Y. Liang, Z. Cui, F. Meng, L. Chen, Z. Wang, T. Yu, C. Liu, The mechanism and machinability of laser-assisted machining zirconia ceramics, *Ceram. Int.* 49 (2023) 16971–16984, <https://doi.org/10.1016/j.ceramint.2023.02.059>.
- [49] X.Z. Zhang, T.J. Chen, Y.H. Qin, Effects of solution treatment on tensile properties and strengthening mechanisms of SiCp/6061Al composites fabricated by powder thixoforming, *Mater. Des.* 99 (2016) 182–192, <https://doi.org/10.1016/j.matdes.2016.03.068>.
- [50] X. Jiao, J. Wang, C. Wang, Z. Gong, X. Pang, S.M. Xiong, Effect of laser scanning speed on microstructure and wear properties of T15M cladding coating fabricated by laser cladding technology, *Opt. Lasers Eng.* 110 (2018) 163–171, <https://doi.org/10.1016/j.optlaseng.2018.05.024>.
- [51] D.F.S. Ferreira, J.S. Vieira, S.P. Rodrigues, G. Miranda, F.J. Oliveira, J.M. Oliveira, Dry sliding wear and mechanical behaviour of selective laser melting processed 18Ni300 and H13 steels for moulds, *Wear* (2022) 488–489, <https://doi.org/10.1016/j.wear.2021.204179>.
- [52] Y. Guo, C. Li, M. Zeng, J. Wang, P. Deng, Y. Wang, In-situ TiC reinforced CoCrCuFeNiSiO₂ high-entropy alloy coatings designed for enhanced wear performance by laser cladding, *Mater. Chem. Phys.* 242 (2020), <https://doi.org/10.1016/j.matchemphys.2019.122522>.
- [53] G. Prabu, N. Jeyaprakash, C.H. Yang, I.A. Alnaser, Evaluation of friction and wear depth during the cyclic loading on partly melted LPBF particles of LPBF cu alloy, *Mater. Charact.* 217 (2024), <https://doi.org/10.1016/j.matchar.2024.114386>.
- [54] T. El-Raghy, P. Blau, M.W. Barsoum, Effect of grain size on friction and sliding wear of oxide ceramics, *Wear* 162–164 (1993) 269–279, [https://doi.org/10.1016/0043-1648\(93\)90509-K](https://doi.org/10.1016/0043-1648(93)90509-K).
- [55] H. Figiel, O. Zogal, V. Yartys, TiB₂- and Fe₂P with nanotwins-reinforced cu-based immiscible composites fabricated by selective laser melting: formation mechanism and wear behavior, *J. Alloys Compd.* 404–406 (2005) 1, <https://doi.org/10.1016/j.jallcom.2005.05.002>.